AD_____

Award Number: W81XWH-04-1-0240

TITLE: High Resolution Anatomic and Elastographic Transrectal Ultrasound for Improved Diagnosis of Prostate Cancer

PRINCIPAL INVESTIGATOR: John A. Hossack, Ph.D.

CONTRACTING ORGANIZATION: University of Virginia
                                                Charlottesville VA 22904

REPORT DATE: February 2007

TYPE OF REPORT: Annual

PREPARED FOR: U.S. Army Medical Research and Materiel Command
                         Fort Detrick, Maryland 21702-5012

REPORT DOCUMENTATION PAGE

Form Approved
OMB No. 0704-0188

1. REPORT DATE *(DD-MM-YYYY)*	2. REPORT TYPE	3. DATES COVERED *(From - To)*
01-02-2007	Annual	21 Jan 06 – 20 Jan 07

4. TITLE AND SUBTITLE

High Resolution Anatomic and Elastographic Transrectal Ultrasound for Improved Diagnosis of Prostate Cancer

5a. CONTRACT NUMBER

5b. GRANT NUMBER
W81XWH-04-1-0240

5c. PROGRAM ELEMENT NUMBER

6. AUTHOR(S)
John A. Hossack, Ph.D.

E-Mail: jh7fj@virginia.edu

5d. PROJECT NUMBER

5e. TASK NUMBER

5f. WORK UNIT NUMBER

7. PERFORMING ORGANIZATION NAME(S) AND ADDRESS(ES)

University of Virginia
Charlottesville VA 22904

8. PERFORMING ORGANIZATION REPORT NUMBER

9. SPONSORING / MONITORING AGENCY NAME(S) AND ADDRESS(ES)
U.S. Army Medical Research and Materiel Command
Fort Detrick, Maryland 21702-5012

10. SPONSOR/MONITOR'S ACRONYM(S)

11. SPONSOR/MONITOR'S REPORT NUMBER(S)

12. DISTRIBUTION / AVAILABILITY STATEMENT
Approved for Public Release; Distribution Unlimited

13. SUPPLEMENTARY NOTES

14. ABSTRACT

In this work we improve upon conventional Digital Rectal Examination (DRE) and PSA blood test by using ultrasound elasticity imaging. A latex sheath over the transrectal ultrasound probe is slightly inflated with water to provide a source of moderate pressure. The elasticity image is generated by cross-correlating successive raw radio frequency image data sets for incrementally increasing pressure. Strain, and consequently elasticity, can be calculated from the displacement image. Our second objective is to use a new freehand 3D acquisition approach to obtain 3D image data sets. This approach uses a slightly modified transducer and an image motion tracking technique. Preliminary phantom based results are presented in this report. Excellent progress has been made with respect to the Statement of Work and first three of four total Specific Aims. A transducer has been specified and is on order. As promised, this transducer is designed to possess unsurpassed prostate scanning resolution by virtue of its exceptionally high frequency – up to 14 MHz. Prototype phantoms and complete ultrasound test instrumentation has been assembled. Preliminary ultrasound image speckle reduction work has been performed. Preliminary, dimensionally accurate, 3D prostate phantom images have been produced.

15. SUBJECT TERMS
ultrasound, imaging, diagnostic, elastography, 3D imaging, image processing

16. SECURITY CLASSIFICATION OF:			17. LIMITATION OF ABSTRACT	18. NUMBER OF PAGES	19a. NAME OF RESPONSIBLE PERSON USAMRMC
a. REPORT	**b. ABSTRACT**	**c. THIS PAGE**	UU	38	**19b. TELEPHONE NUMBER** *(include area code)*
U	U	U			

Standard Form 298 (Rev. 8-98)
Prescribed by ANSI Std. Z39.18

Table of Contents

INTRODUCTION

The American Cancer Society estimated that there would be approximately 230,110 new cases diagnosed and approximately 29,900 prostate cancer related deaths in 2004 (American Cancer Society 2004) Prostate cancer screening today generally uses the Prostate Specific Antigen (PSA) blood testing, free PSA testing and Digital Rectal Examination (DRE). When using a 'cutoff' of PSA > 4.0 ng/mL and an abnormal DRE, sensitivity, specificity and Positive Predictive Value (PPV) are 38%, 88% and 56% respectively (Crawford, Leewansangtong et al. 1999). When either an elevated PSA or an abnormal DRE are used, (in isolation – not in combination), sensitivity, specificity and PPV are even lower (Crawford, Leewansangtong et al. 1999). When the PSA is used there exists a significant gray area (4 - 10 ng/mL) in which cancers may be missed and yet the number of negative biopsies is large. Even though cancer detection sensitivity, specificity and PPV are improved by combining PSA and DRE (Toubert, Schlageter et al. 1990; Crawford, Leewansangtong et al. 1999) the usefulness of DRE remains fundamentally limited due to its subjective nature. Additionally, DRE is practically limited to the detection of shallow (subcapsular) palpable abnormalities. Even systematic multi-core biopsy fails to detect clinically detectable cancers in up to 34% of men (Frauscher, Klauser et al. 2001). However, there is evidence that as additional biopsies cores are added, sensitivity improves (Taylor, Gancarczyk et al. 2002). This observation has resulted in an increase the number of cores taken during routine examination. Nevertheless, biopsy-based detection sensitivity remains less than ideal. Thus, there is plenty of compelling clinical interest in finding improved methods for the early diagnosis of prostate cancer with improved sensitivity and specificity. One recent example of progress in the field of prostate cancer detection involves an effort to automate the DRE examination. Savazyan recently described a system for 'mechanical imaging' of the prostate (Sarvazyan 1998). This system comprises a rectal probe that is instrumented with an array of pressure sensing strain gages and a 3D magnetic positioner device. In an *in vitro* trial (Weiss, Hartanto et al. 2001), the new system correctly detected and located 100% of the nodules under examination. This compares with detection rates of 83% and 67% for an experienced urologist and a student respectively. Thus, a significant improvement over the conventional DRE examination has been demonstrated for the *in vitro* case. Another recent development is the observation that the sensitivity of an ultrasound examination can be improved by the use of a microbubble based contrast agents (Frauscher, Klauser et al. 2001). Frauscher's approach (Frauscher, Klauser et al. 2001) involved the use of contrast agent enhanced Color Doppler that improved the detection of hypervascular regions associated cancer. Prostate cancer was detected by contrast agent assisted ultrasound in 23 of 24 patients known to have prostate cancer. (The method used for determining definitively which patients had cancer is not entirely clear in the article.) In comparison, conventional ultrasound detected cancer in 17 patients. The contrast agent assisted approach detected cancer in 8 patients with a negative systematic biopsy-based diagnosis. However, the cost of the contrast agent used in this study was $65 per patient. This cost makes up approximately half of the cost of a conventional ultrasound examination and therefore represents a considerable impediment to its widespread acceptance. However, more recent publications (Clements 2002; Halpern, McCue et al. 2002) (including one from Frauscher's group) cast doubt on the true extent of the improvement in diagnostic accuracy obtained by using contrast agents. Specifically, Halpern was unable to detect cancers in the inner gland and achieved a cancer detection sensitivity of only 42% (Halpern, McCue et al. 2002).

BODY

The work conducted as part of this Army funded program can be considered as divided into the following key "Aims":

1. Research, design, development and prototype testing of a new transrectal ultrasound transducer, syringe pump and ultrasound instrumentation to facilitate a Synthetic Digital Rectal Examination (SDRE).
2. Research, development and prototype testing of techniques to enable quantitative (dimensionally accurate) 3D reconstructions of the prostate
3. Research, development and test of techniques to improve ultrasound image quality and to facilitate automated (or semi-automated) border detection of lesions
4. Small scale clinical test at the University of Virginia

Progress has been made in each of these tasks in the third year of the grant.

Progress with respect to the areas are related directly to the committed Statement of Work that was funded:

Aim 1. Design, specify, and have built, a high resolution transducer optimized for imaging elastic inhomogeneities, unsurpassed B-Mode image resolution and possessing integrated 3D capability.
A high frequency (8-14 MHz) transducer array was designed and specified in Year 1. In 2005, the transducer was manufactured and delivered by Vermon SA, Tours, France. This specialized ultrasound transducer has two tracking arrays each with 32 elements, a central imaging array with 192 elements and the elements are spaced on a 0.2 mm pitch. This transducer is providing superb imaging resolution in a transducer housing specially designed for transrectal ultrasound. The transducer has provided the high quality raw ultrasound data as a basis for the subsequent work elements. This transducer is operable at up to 14MHz whereas the previously available transducer was only operable up to 8 MHz. Consequently, we obtain excellent, and significantly improved, image resolution.

Aim 2. Develop and test a tissue elasticity imaging system.
We assembled the apparatus to enable the new approach to transrectal ultrasound based strain imaging in Year 1 and Year 2. We have also made several custom prostate phantoms using locally developed techniques (Negron, Viola et al. 2002). Using internally made phantoms, we have been able to iterate efficiently the design and also to fabricate replacement phantoms at low cost in a timely manner. Phantoms generally deteriorate over time due to dehydration through the membranes. We have tested the tissue elasticity system using both an older 8 MHz transrectal transducer and the newer 14 MHz transducer connected to our Siemens Sequoia ultrasound machine. (Our techniques can be migrated to other ultrasound systems if resource and contractual issues are addressed.)

We spent a considerable portion of Year 3 working on improved algorithms for 3D elastography and image processing. This is described below:

Multi-resolution hybrid strain estimator

Time delay estimation has been extensively reported in the literature as an effective method to estimate blood flow (Kasai et al. 1985) and tissue motion (Chen et al. 1992). In the field of elastography, O'Donnell et al. (1994)) have used the zero-crossing of the phase of the complex cross correlation function (base band signal) to estimate tissue strain, whereas Konofagou et al. (2000a) have used shift in the power spectrum of the pre- and post-compression echo RF signal to estimate tissue strain. Bilgen (1999) has reported a wavelet based direct strain estimator (no gradient operation) for elastography. In this section, we describe a multistage hybrid adaptive displacement (and strain) estimation algorithm. Figure 1 illustrates the complete flow chart of this strain estimation algorithm, which is elaborated in the following paragraphs. In strain estimation, cross-correlation between pre- and post-compression signals is maximized when two signals are jointly stationary. In addition, if the time-bandwidth product is large and the shifts in the signal are small, cross-correlation is an efficient estimator of displacement (hence strain) and in the limit achieves the Cramer-Rao lower bound on variance (Walker and Trahey 1995). However, in practice, pre- and post-compression signals are jointly non-stationary. Hence, signal companding (Chaturvedi at al. 1999) or stretching (Céspedes and Ophir 1993) is frequently used to improve image quality. However, for global stretching to be effective, an *a priori* estimate of applied tissue strain is required. In conventional elastography, a calibrated and computer controlled motion stage is used to apply an external displacement, it accurately determines the applied displacement at the top surface of the object being compressed due to uniform compression. Hence, the applied strain at the top of the compressed object is known *a priori*. In hand-held and trans-rectal prostate elastography, applied displacement cannot be guessed *a priori* as the applied compressions are not calibrated or controlled. In addition, the strain induced in the compressed object decays or attenuates with depth, and is governed by non- uniform[1] boundary conditions.

---

[1] When the compressor plate is smaller in dimension than that of the compressed homogeneous object, the stress distribution in the object is non-uniform and is referred to as non-uniform boundary condition at the object boundary (Shapo et al. 1996,).
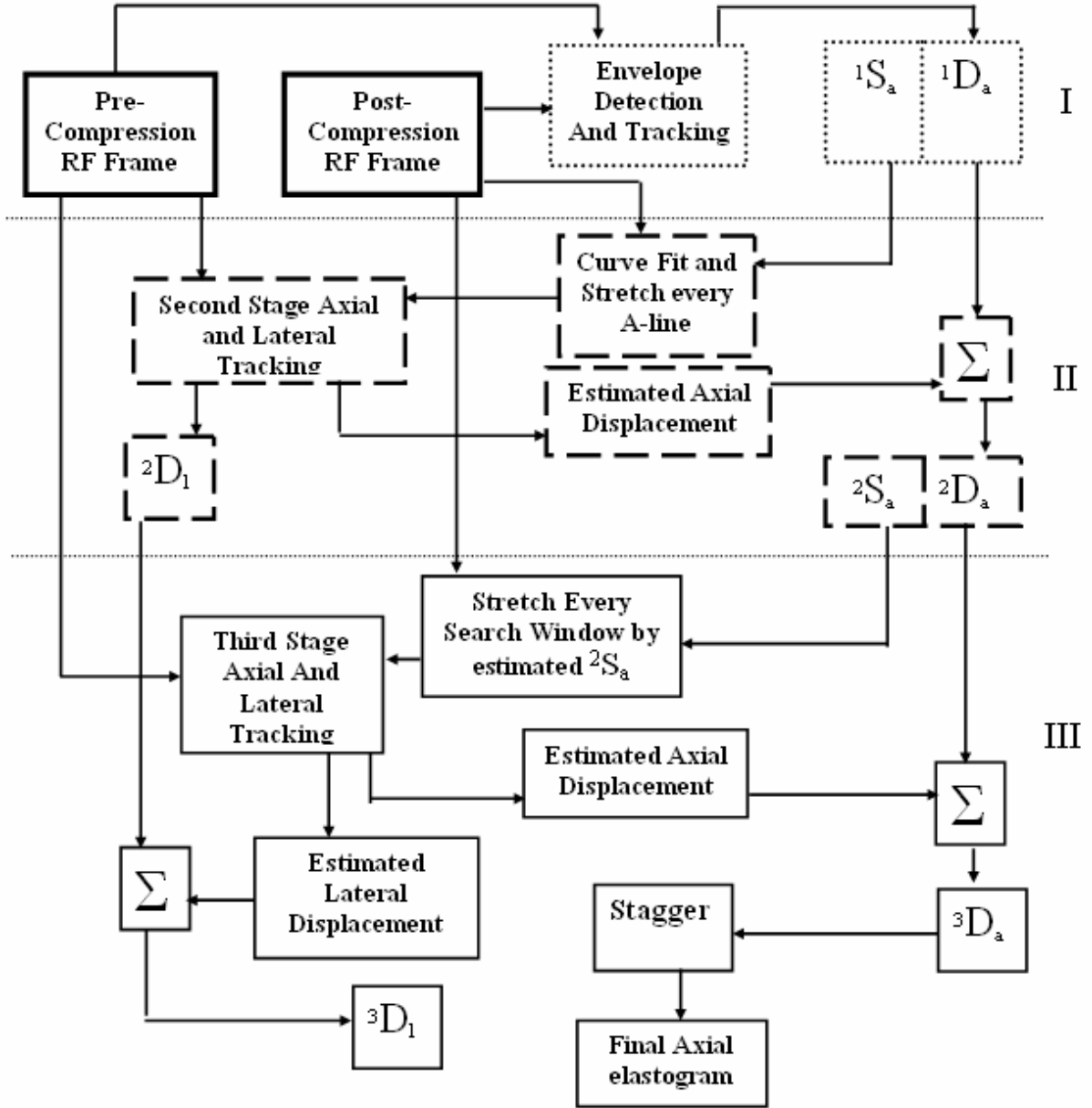
Figure 1: Flow chart of the new strain estimation algorithm. Note: dotted lined-rectangular boxes denote first-stage (I), whereas, dashed lined-rectangular boxes signify second-stage (II), and solid lined-rectangular boxes represent third-stage (III).

Hence, uniform global stretching in the first stage of any adaptive strain estimation algorithm (Srinivasan et al. 2002b) may produce sub-optimal results. Also, when applied strain is large (> 2%, for a ~4 cm deep prostate tissue imaged at 12 MHz), the induced displacement is sufficiently larger than the wavelength corresponding to center frequency and may introduce ambiguity in peak detection of the cross-correlation function obtained by tracking the pre- and post-compression RF data. Hence, in the first stage of our algorithm, we demodulate the RF data and track the envelope of the pre- and post-compression echo RF frames to yield average "first-guess" strain estimates over the tracking window-W. The window, W, is the spatial length of the kernel over which the pre- and the post-compression signal cross-correlation is carried out. The window in this stage is larger than in the subsequent RF tracking stages to obtain

estimates with higher SNR. The displacement obtained from this stage is referred to as the first stage axial displacement ($^{1}D_a$), where superscript '1' denotes the stage and subscript 'a' denotes the displacement type (axial

In the second stage, a polynomial curve[2] is fitted to the estimated local strain profile over an A-line, and the corresponding A-line is stretched by the curve-fitted first-stage strain. Srinivasan et al. (2002b) stretched the post-compression data globally by the average applied strain, whereas Chaturvedi et al. (1999) compressed the pre-compression data by the average tissue strain. In either case, the first stage did not take into account the local variations in tissue contrast. In addition, both algorithms require an *a priori* estimate of the applied strain. In the proposed algorithm, signal stretching is performed locally over a tracking window on every A-line, taking account of the local variation in tissue elasticity without any *a priori* knowledge of the applied tissue strain. Lateral displacement ($^{2}D_l$) is estimated by performing lateral tracking (Konofagou et al. 2000b). The pre- and the stretched post-compression echo RF data are then tracked to yield a local strain estimate over the search window. The axial displacement estimated in this stage is added to the first stage axial displacement and the resultant axial displacement is referred to as the second stage axial displacement ($^{2}D_a$).

The third stage is used to estimate residual strain. In the third stage, the original un-stretched post-compression RF data are stretched locally over a tracking window using the estimated second-stage strain. The stretched post-compression data are then tracked with the pre-compression data to yield residual axial displacements. The lateral displacements are obtained by tracking the A-lines laterally. When performing lateral tracking, the search window in the pre-compression data is tracked with the corresponding window on adjacent A-lines in the post-compression data. The maximum cross-correlation coefficients over these windows are estimated and a cosine curve (cosine interpolation) (Céspedes and Ophir 1993) is fitted to the data points. The shift in the peak of this curve in the transverse (lateral or azimuthal) direction yields the lateral displacement of the local post-compression window. The axial and lateral displacements estimated in this stage are added to the second stage axial and lateral displacement to yield the final axial ($^{3}D_a$), and lateral displacements ($^{3}D_l$). The gradient of the axial displacement image yields a strain image, but gradient operator is a high pass operator and amplifies noise. A least square estimator may be applied to a displacement image to produce a smooth elastogram, but the losses in tissue contrast and resolution may be substantial (Kallel and Ophir 1997). A staggered strain operator (Srinivasan et al. 2002a) limits noise amplification and provides smooth elastograms while minimizing the loss in contrast and resolution. Hence, in the last step of this algorithm, we apply staggered strain estimation technique to the final stage axial displacement image to generate a final stage elastogram. In principle, the staggering estimator performs a band-pass filtering operation partially mitigating the noise-enhancing effect of the high pass filtering resulting from the gradient operator.

---

[2] The estimated first stage strain profile is interpolated using cosine interpolation to match the sampling rate of the RF data.

3D Elastographic simulation framework

An elastographic simulation framework similar to that proposed by Nightingale et al. (2000) and Patil et al. (2006) was used to in this work. Patil et al. had used a 3D shift-invariant convolution model for generating the pre- and post compression echo RF data. In this work, we have used a more realistic Field II simulation model (Jensen and Nikolov 2000) for echo RF data generation. Most FEA simulations performed by Patil et al. were restricted by the assumption of uniform boundary conditions, which is not strictly valid for transrectal prostate elastography. In this work, all FEA simulations were performed with non-uniform boundary conditions. Figure 2 illustrates the flow diagram of the simulation framework used in this work. ANSYS (Canonsburg, PA), a finite element analysis (FEA) simulation software package, was used in this work. Arbitrary regions of interest (ROI's) can be created within the FEA model by changing the local material properties (shear modulus, material density etc.). A fine FEA mesh (approximately 13 FEA nodes per resolution cell) results in accurate parameter estimation (3D internal displacement, in this case). Boundary conditions (applied displacement) can be applied to an object surface, an object element, or a node of the object element (after meshing). The internal object deformation due to the applied displacement is then estimated by solving the associated partial differential equations numerically. In this work, a preconditioned conjugate gradient iterative solver was chosen to perform numerical simulations (Elman 1981). This solver was chosen because it provided similar performance as compared with the other solvers (within ANSYS) at a relatively small computational time (Patil 2005). A grid of scatterers was defined over the 3D ROI of the simulated object (48 scatterers per resolution cell (Walker 2006)). The post-compression scatterer position was simulated by applying the 3D displacement field obtained from the FEA software to the scatterers.
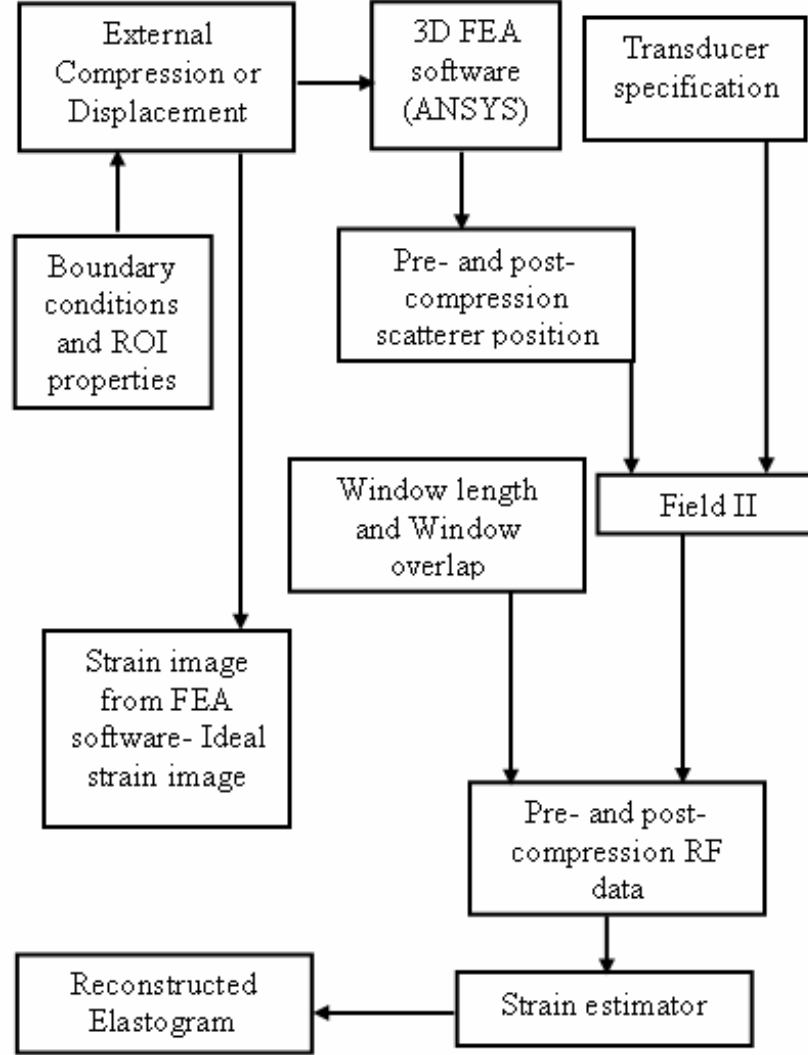
Figure 2: 3D elastographic simulation framework .

It is worthwhile noting that the FEA simulations accounted not only for translational but also for rotational motion of an object due to any arbitrary boundary condition. Thus, realistic tissue motions can be simulated for arbitrary boundary conditions and arbitrary object shapes. Field II simulations were used to generate the pre- and post-compression echo RF data. The generated pre- and post-compression data can be tracked using different displacement (strain) estimation algorithms to generate a strain image. In this work, we used the strain estimation (signal processing) algorithm detailed in section 2.

Performance evaluation of the strain estimator using 3D elastographic simulations and experiments

  A. Simulations

Elastographic simulations were performed using the framework described in section 3. Table 1 lists the simulation parameters used for performing various simulations described in this section.
Table 1 Simulation parameters .

Entity	Value
Dimensions of background	40x40x40 mm cube
Modulus ratio of inclusion and background	3
Approximate diameter of the inclusion	10 mm
Center frequency of scan	12 MHz
Sampling frequency	80 MHz
System SNR	30 dB
1D linear array	192 elements, 0.2 mm pitch
Focus	20 mm
Fractional bandwidth	40%
Window length (W)	2 mm
Overlap	90%

A cube (40 x 40 x 40 mm) enclosing a spiculated inclusion (10 mm diameter) was used as a mechanical model to simulate the background and the lesion (Figure 3). The embedded inclusion (Young's Modulus=12 KPa) was simulated to be three times stiffer than the background (Young's Modulus=4 KPa). A uniform cube was used for the SNR study. The cubes were compressed axially from the top and assumed to be rested on a fixed surface such that their motions in the lateral and elevational directions were unconstrained (slip conditions). The cubes were compressed along the elevational axis of symmetry using a compressor plate (40 x 3 mm- lateral elevation plane) and the transducer array was placed over the compressor plate. The surface area of the compressor plate was smaller than the surface area of the top of the cube to simulate non-uniform boundary conditions at the top surface of the cube (Figure 3). This results in non-uniform stress distribution through the depth of the tissue and consequently causes strain decay. The cube was subjected to a range of applied strain (0.5-10%). ANSYS was used to perform these simulations. The transducer was focused at 20 mm (range or axial direction). RF data were generated using the 3D elastographic simulation framework as described in section 3
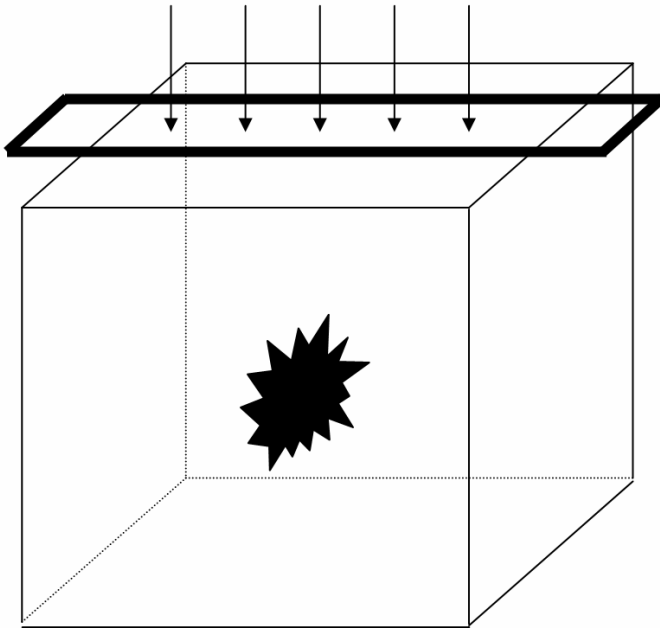

Figure 3: Schematic of the simulated phantom and imaging array used for CNR$_e$ study. The cube is 40x40x40 mm and the compressor plate is 40x 3 mm.

The generated pre- and post-compression RF data were tracked using: 1) the proposed algorithm, 2) the algorithm proposed by Srinivasan et al. (2002b), and c) 1D RF data tracking using uniform global stretching (Céspedes and Ophir 1993). Signal-to-noise ratio (O'Donnell et al. 1994) and contrast-to-noise ratio (Bilgen and Insana 1997) were used as metrics for comparing the above listed tracking algorithms. Figures 4 through 7 illustrate the first, second and final stage elastograms obtained using the proposed algorithm. Figure 8 illustrates the numerical strain image obtained from 3D FEA simulation
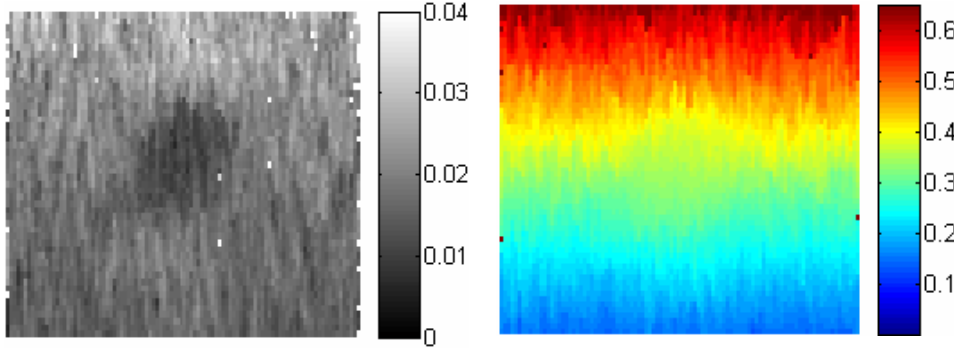
Figure 4: First stage elastogram (Left) and axial displacement image (Right). The field of view is 40x40 mm. The images were obtained using parameters specified in Table 1.
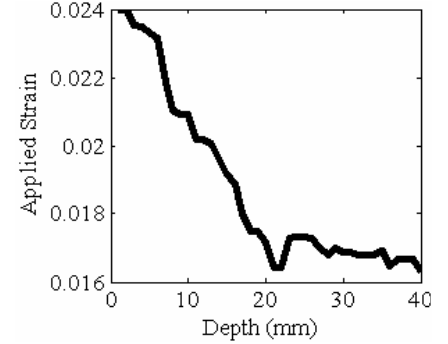
Figure 5: Strain profile over an A-line in the elastogram (Figure 4-Left) obtained by the B-mode tracking.
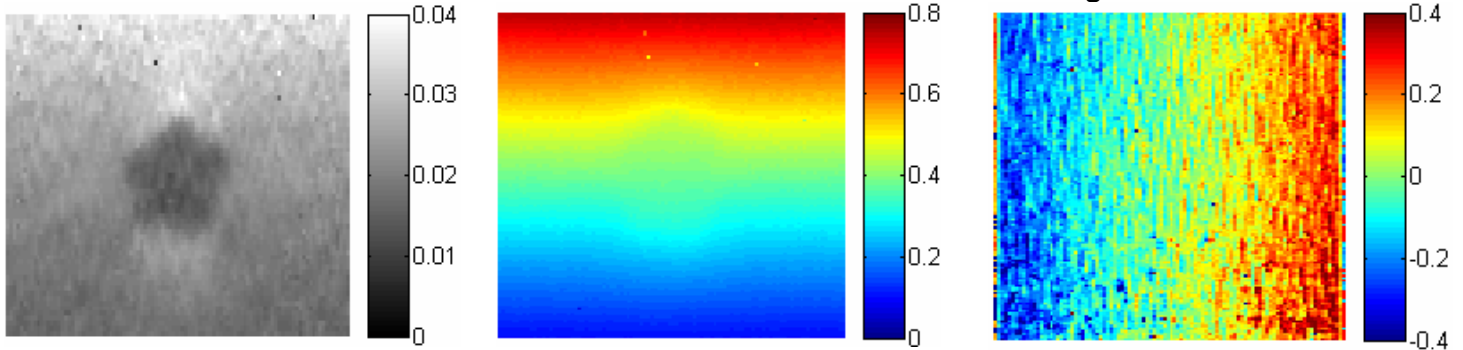

Figure 6: Second stage elastogram (Left), axial displacement image (Center), lateral displacement image (Right). The field of view is 40x40 mm. The images were obtained using parameters specified in Table 1.
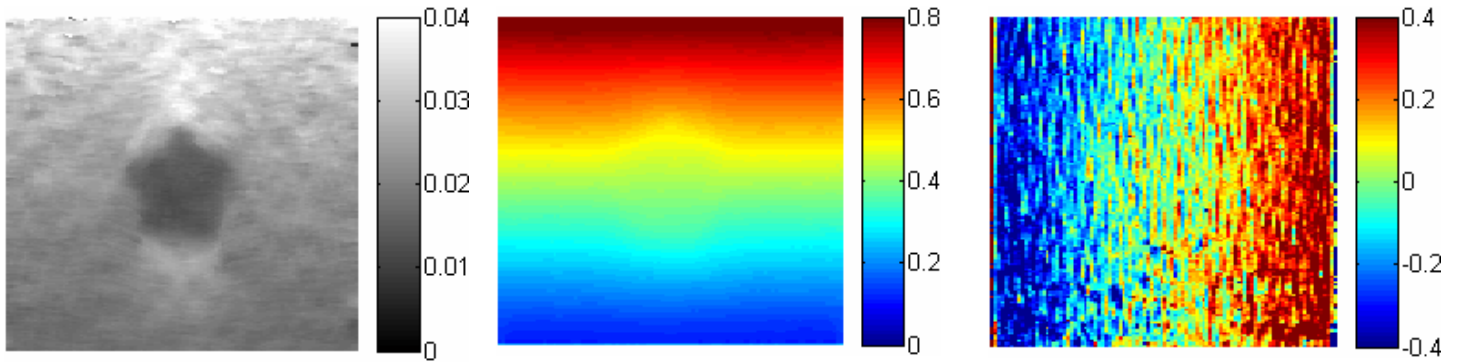

Figure 7: Final stage elastogram (Left), axial displacement image (Center), lateral displacement image (Right). The field of view is 40x40 mm. The images were obtained using parameters specified in Table
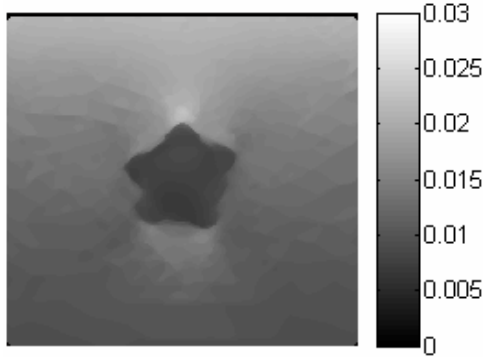
1.

Figure 8: Ideal strain image obtained from the FEA simulations. The image was obtained using non-uniform boundary conditions, other mechanical parameters used in FEA simulations are listed in Table 1.

Figure 9 illustrates the theoretical elastographic SNR (SNR_e) plot obtained using the specifications of the simulated transducer and the aforementioned signal processing parameters. The theoretical framework proposed by Varghese and Ophir (1997) was used for generating the theoretical SNR_e curve plot. It is important to note that the theoretical SNR_e curve: 1) assumes one dimensional speckle motion, and 2) joint stationarity of pre- and post-compression signals, 3) neglects frequency dependent attenuation and 4) assumes that the observation window is at the focus of the transducer. In view of these assumptions, the theoretical SNR_e can never be achieved in practice. Nevertheless, the theoretical SNR_e plot can be used as a "gold standard" to evaluate the performance of any strain estimation algorithm. Figure 10 illustrates the signal-to-noise curves estimated using the proposed algorithm and the above listed tracking approaches. Equation (1) was used to estimate the elastographic signal-to-noise ratio (SNR_e) from the reconstructed elastograms (O'Donnell et al. 1994),

$$SNR_e = \frac{s}{\sigma_s} \qquad (1)$$

where s is the average strain estimated over the entire image. σ_s is the variance of strain estimates. The SNR_e curve estimated using the proposed algorithm envelopes the SNR_e curves obtained using the global stretching-based RF data tracking algorithm and the algorithm by Srinivasan et al. (2002b). For all values of applied strain, the SNR_e plot obtained from the proposed algorithm was statistically different ($p < 0.05$) from the one obtained using the algorithm proposed by Srinivasan et al. (2002b). Analysis of variance was used as a statistical measure for quantifying the differences between the two SNR_e curves. Thirty independent realizations were used for the statistical study. Figure 11 illustrates the image variance estimated at different values of applied strain. As predicted using strain filter theory (Varghese and Ophir 1997), the variances in strain estimation increase non-linearly with applied strain. The rate of increase in variance is lowest when using the proposed algorithm. Figure 12 illustrates the average cross-correlation coefficient (ρ) over the image obtained using different tracking algorithms. The cross-correlation coefficient obtained by tracking the pre- and the post-compression signal can be expressed analytically as:

$$\rho_{ps} = \frac{\sigma_{ps}}{\sqrt{\sigma^2_p \sigma^2_s}}, \qquad (2)$$

where

$$\sigma_{ps} = \int_{-T/2}^{T/2} S_p(t) S_s(t+\tau)dt, \qquad (3)$$

(4)

(5)

$$\sigma^2{}_p = \int_{-T/2}^{T/2} S^2{}_p(t)dt \quad \text{, and}$$

$$\sigma^2{}_s = \int_{-T/2}^{T/2} S^2{}_s(t)dt.$$

Subscript p denotes pre-compression and s denotes post-compression (O'Donnell et al. 1994). T is the tracking window ($W = T*c/2$); c is the speed of sound through the tissue. ρ_{ps} is the cross-correlation coefficient. The error bars in Figure 12 illustrate the variance in the average image cross-correlation coefficient obtained from thirty independent realizations. The rate of decrease in the correlation coefficient as a function of applied strain is smallest for the proposed algorithm. Figure 13 illustrates different contrast-to-noise ratio curves- CNR_e (Bilgen and Insana 1997) obtained from the elastograms simulated using different strain estimation algorithms. Contrast-to-noise ratio is expressed as,

$$CNR_e = \frac{abs(s_t - s_b)}{\sqrt{\dfrac{\sigma^2{}_t + \sigma_b{}^2}{2}}} \tag{6}$$

where, s_t is the average strain in the target, and s_b is the average strain of the background. $\sigma^2{}_t$ is the variance of the strain estimates in the target, and $\sigma^2{}_b$ is the variance of the strain estimates in the background. CNR_e values for a range of applied strain (0.5-10%) obtained using the proposed algorithm are 3 dB above the CNR_e curve obtained using the algorithm proposed by Srinivasan et al.(2002b) and are 6 dB higher than the RF data tracking algorithm with uniform global stretching (Céspedes and Ophir 1993).
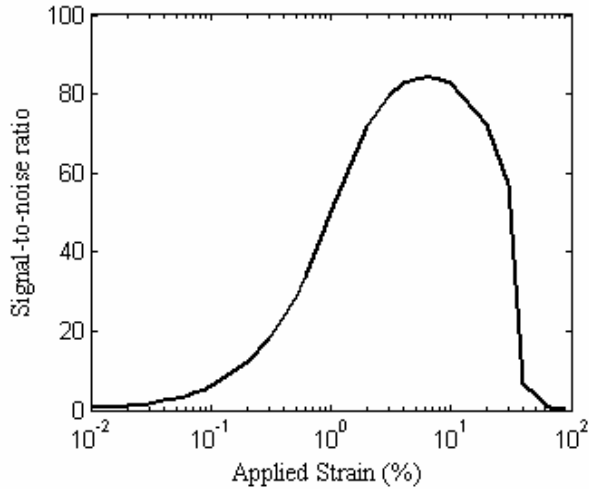

Figure 9: Theoretical SNR$_e$ plot for a range of applied strains. The plot was obtained at 12 MHz center frequency, 40 % fractional bandwidth (-6 dB), system SNR of 30 dB, window length of 2 mm and overlap of 90 %.
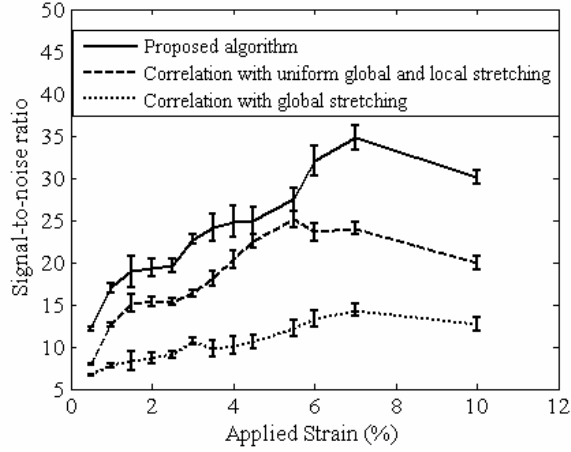
Figure 10: SNR$_e$ plots comparing proposed algorithm with uniform global stretching only (Céspedes and Ophir 1993), and global followed by local stretching approaches (Srinivasan et al. 2002b).
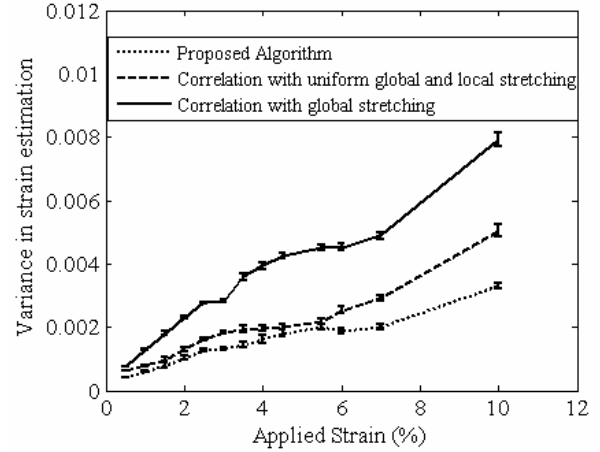

Figure 11: Estimated image variance comparing proposed algorithm with uniform global stretching only (Céspedes and Ophir 1993), and global followed by local stretching approaches (Srinivasan et al. 2002b).
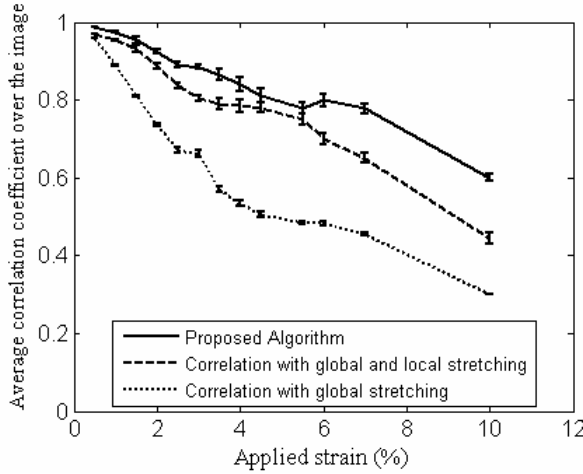

Figure 12: Average cross-correlation coefficient over the reconstructed image obtained using proposed algorithm, algorithm with uniform global stretching only (Céspedes and Ophir 1993), and global followed by local stretching approaches (Srinivasan et al. 2002b).

Figure 13: CNR$_e$ ratio plots obtained using proposed algorithm, algorithm with uniform global stretching only (Céspedes and Ophir 1993), and global followed by local stretching approaches (Srinivasan et al. 2002b).
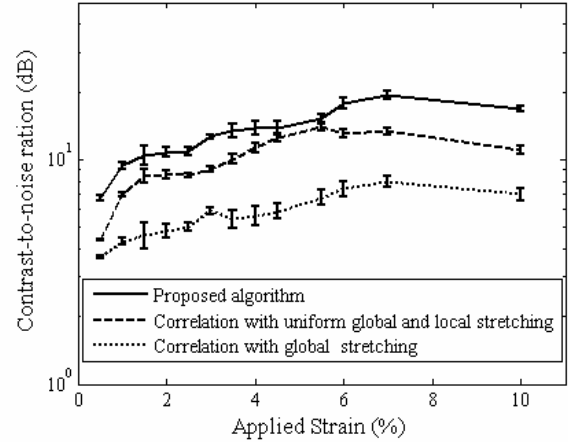
B. Experiments

Experimental evaluation of the tracking algorithm was performed on an acryl-amide based prostate phantom previously fabricated by (Li et al. 2005). The mean cross-sectional diameter of the embedded oblong inclusion in the longitudinal (range) direction was approximately 7 mm. A Siemens Sequoia 512 scanner (Siemens Medical Solutions, Mountain View, CA) was used in this study. Multiple demodulated "I/Q" (In-phase/Quadrature) radio frequency beamformed lines of acoustic data were acquired from the ultrasound scanner using a research interface employing an I/Q data capture board. A 192 element, 12 MHz, -6 dB 40 % fractional-bandwidth transrectal ultrasound transducer was used for scanning the prostate phantom. The depth of acquisition was 24 mm and the width of acquisition was 40 mm. The experimental apparatus and the protocols used for the validation are described in (Li et al. 2005) and will be reiterated in detail in the phantom experiment section (Section 6). Fifty frames were acquired such that the total applied strain over 50 frames was 2 %. Every 25th frame (1 and 25-$E_{1, 25}$, 2 and 26-$E_{2, 26}$ and so on...) was tracked. Final elastogram was generated by averaging over five independently obtained elastograms (($E_{1, 25}$ +.....+ $E_{5, 29}$)/5) Figure 14a illustrates an elastogram obtained using the method proposed in this paper. Figure 14b illustrates an elastogram reconstructed by using the algorithm proposed by Srinivasan et al. in (2002b). As illustrated in Figures 14a and 14b, elastograms generated by the algorithm proposed in this paper provide higher CNR_e and retain the shape of the enclosed inclusion. The depth dependent strain attenuation is clearly visible in the elastograms in Figures 14a and 14b. Thus uniform global stretching over the entire image as suggested in the first stage of the algorithm by Srinivasan et al. (2002b) results in stretching inaccuracies and is a likely cause of the noise observed in Figure 14b. The algorithm proposed in this paper stretches every A-line by the local strain profile over that A-line as predicted by the B-mode tracking stage (the first stage of the proposed algorithm). Also, the stretching takes into account the strain decay with depth and hence minimizes noise due to stretching inaccuracies, which are likely to occur due to tissue inhomogeneity. The algorithm by Srinivasan et al. (2002b) requires an *a priori* estimate of the applied strain for stretching the post-compression data, whereas the algorithm proposed in this paper does not have such a requirement. Thus, for trans-rectal, and handheld elastography, the proposed algorithm is expected to exhibit superior performance to algorithm proposed by Srinivasan et al. (2002b). For the case with uniform boundary condition (as in motion stage based elastography, where the applied strain is known *a priori*), we expect that both algorithms should demonstrate similar performance.
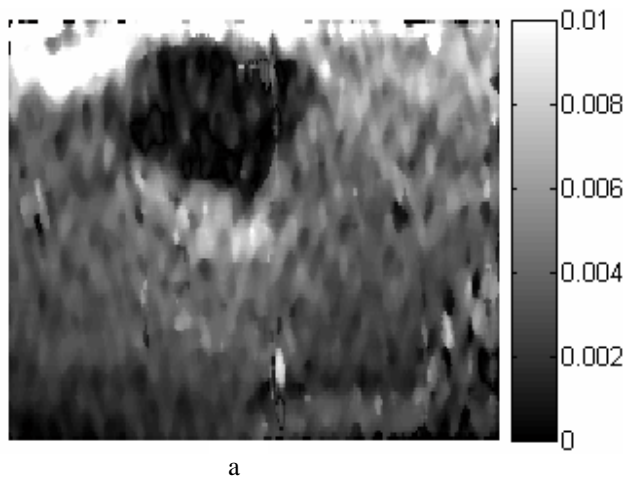

a

b

Figure 14a The modulus contrast ratio of the inclusion in the image with respect to the background was 10. A window length of 2
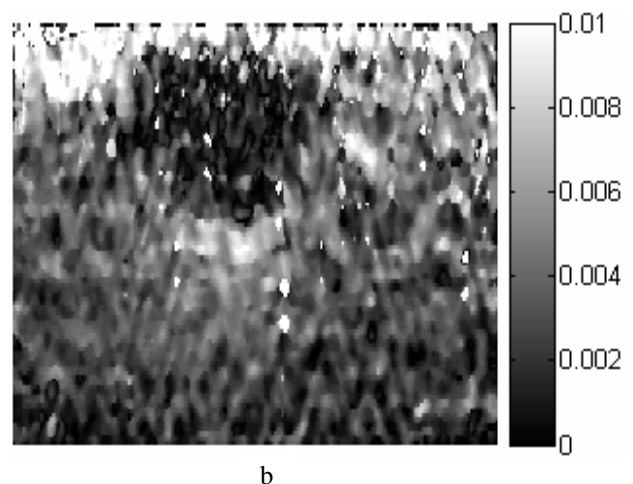
Figure 14b: The modulus contrast ratio of the inclusion in the image with respect to

mm and an overlap of 90 % were used for processing the elastogram. The obtained elastogram is an average strain image over 5 frames. The elastogram was reconstructed using the proposed algorithm.

the background was 10. A window length of 2 mm and an overlap of 90 % were used for processing the elastogram. The obtained elastogram is an average strain image over 5 frames. The elastogram was by reconstructed using the algorithm proposed by Srinivasan et al. (2002b).

1. Rendering 3D shapes of embedded inclusions :Simulations

3D elastographic simulations framework described in section 3 was used for 3D shape rendering study. Two different cases were considered for the 3D rendering study- the axial and the lateral resolution study (Figure 15). The transducer array (Field II) was swept across (along elevation) the inclusions to generate elastograms by 3D rendering. The spiculated inclusion models a malignant lesion, whereas the smooth spherical inclusion models a benign lesion (Ueno 1986, Lee 1988). In the model shown in Figure 15, the background was simulated as a 40x40x40 mm cube with uniform density and stiffness of 4 KPa The inclusion was three times as stiff as the surrounding background. The spherical inclusion had a cross-sectional diameter of 5 mm; whereas the spiculated malignant inclusion had a mean cross-sectional diameter of approximately 6 mm. External displacement was applied to the top surface of the cube as illustrated in Figure 15. Parameters listed in Table 1 were used to for simulations described in this section. The simulated transducer was slowly swept across the top surface of the cube and twenty three pre- and post-compression RF data slices were collected along the elevational dimension. The acquired pre- and post-compression RF data sets were tracked using the algorithm detailed in section 2. Various elastograms obtained along the elevational direction were segmented using 3D gradient vector flow active surface (GVF-AS) algorithm (Tay et al. 2006) and rendered in 3D to reconstruct the 3D shapes of the inclusions. The strain images obtained directly from the FEA simulations were also segmented and rendered to produce ideal 3D shapes of the modeled inclusions. Figure 16 illustrates the 3D reconstruction from the axial resolution study. The modeled malignant and benign lesions were embedded in the 3D cube and were placed longitudinally along the axis of symmetry. The axial separation between the two lesions was reduced in incremental steps of 0.1 mm. For every step, the lesions were reconstructed from the elastograms and rendered in 3D. The process was repeated until the lesions were close enough to each other such that their reconstruction resulted in one fused entity instead of two distinct entities. The axial resolution of the 3D reconstruction was approximately 0.8 mm (five wavelengths). Figure 16-a illustrates a 3D reconstruction from the generated elastograms, whereas Figure 16-b illustrates a 3D reconstruction from the ideal numerical strain images obtained from the FEA simulations. As expected, the 3D reconstruction from ideal images is sharper than that from the elastogram. Also, the lesions reconstructed from the elastogram exhibit shape warping that can be attributed to limitations arising from the signal processing parameters (window length and window overlap etc.), and the non-uniformity of the sampling of the ultrasound data in the three dimensions (Patil et al. 2006). Lateral resolution of the 3D reconstruction was estimated by repeating the steps detailed for the axial resolution study. The lateral resolution of the 3D reconstruction was approximately 1.5 mm (ten wavelengths). Figures 17 a-b illustrate a 3D reconstruction from the lateral resolution study
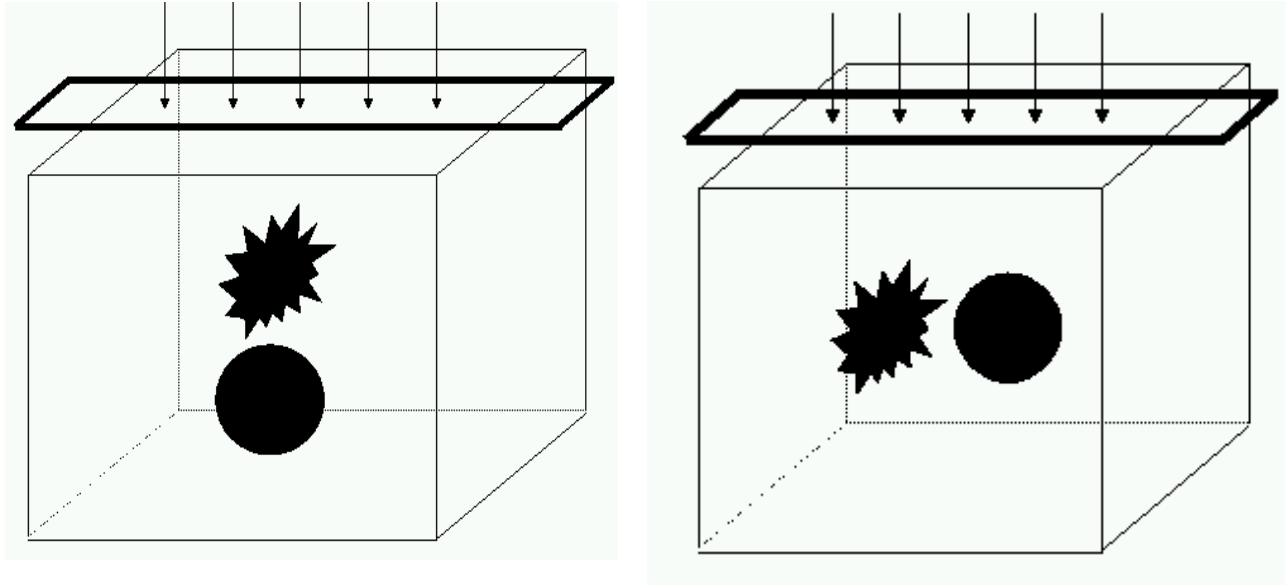
Figure 15: The a ve figures illustrate the two different simula b cases considered for the 3D rendering study. The arbitrary shaped inclusion models a malignant lesion, whereas the smooth spherical inclusion models a benign lesion (Ueno 1986, Lee 1988). The cases a and b were considered to evaluate the axial and the lateral resolution of the 3D reconstruction.
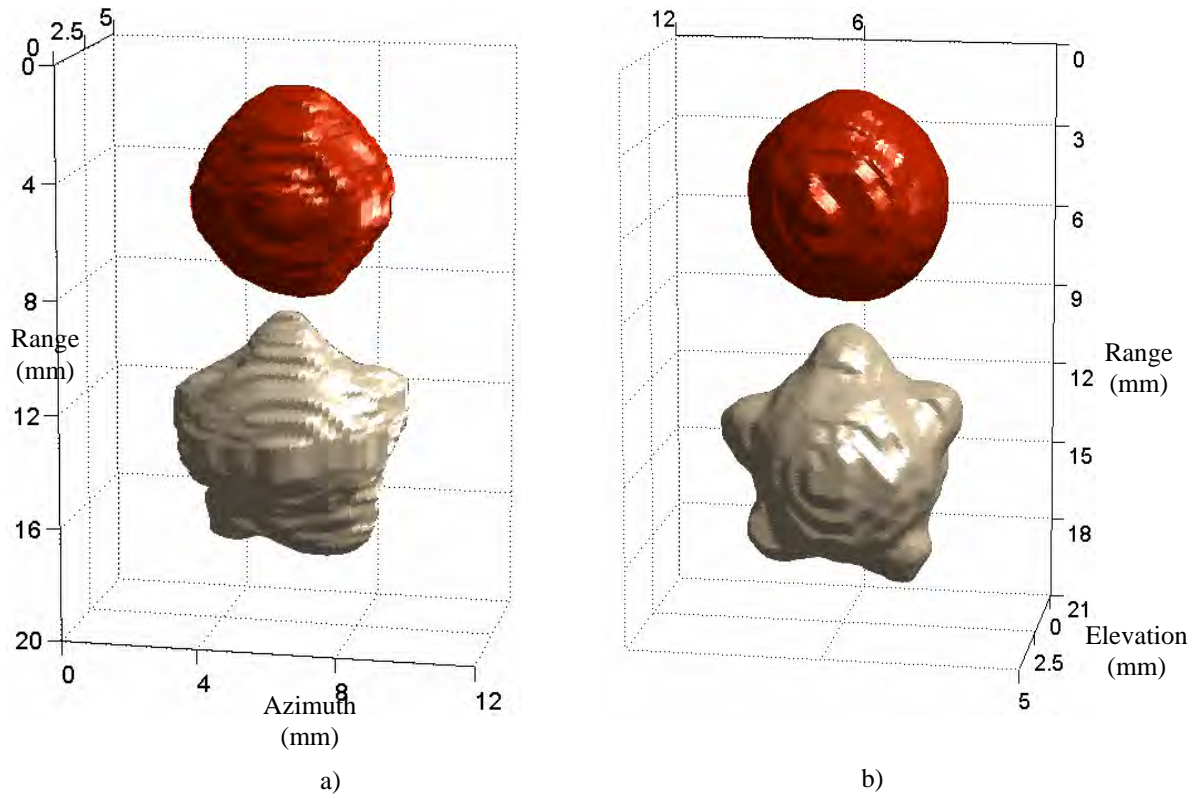
.

Elevation
(mm)

Azimuth
(mm)

Figure 16: Axial resolution simulation study: (a) 3D reconstruction from the reconstructed elastograms, (b) 3D reconstruction from the numerical strain images derived from the FEA simulations
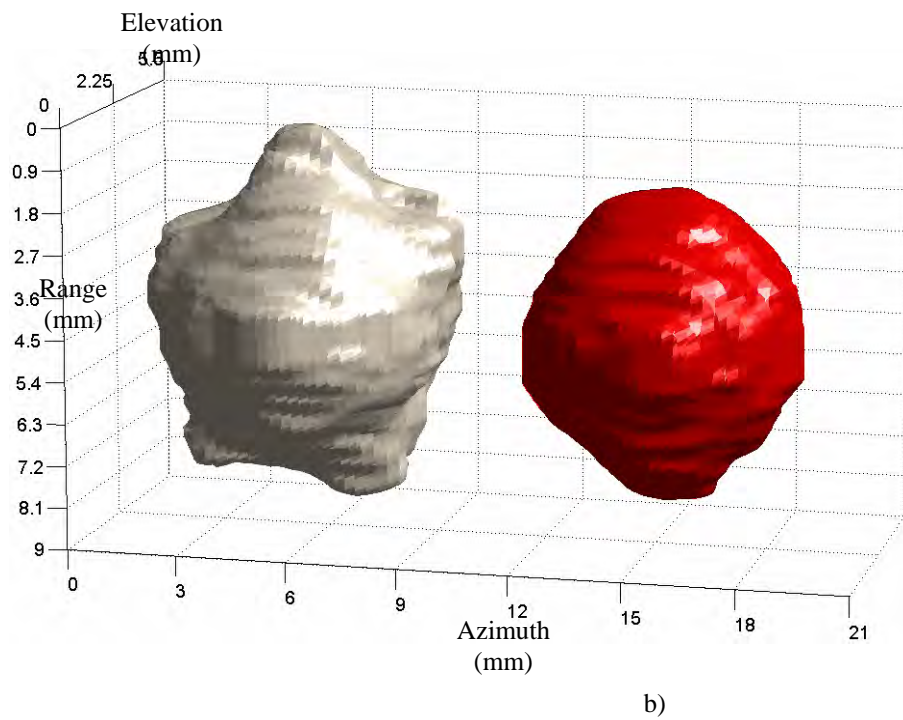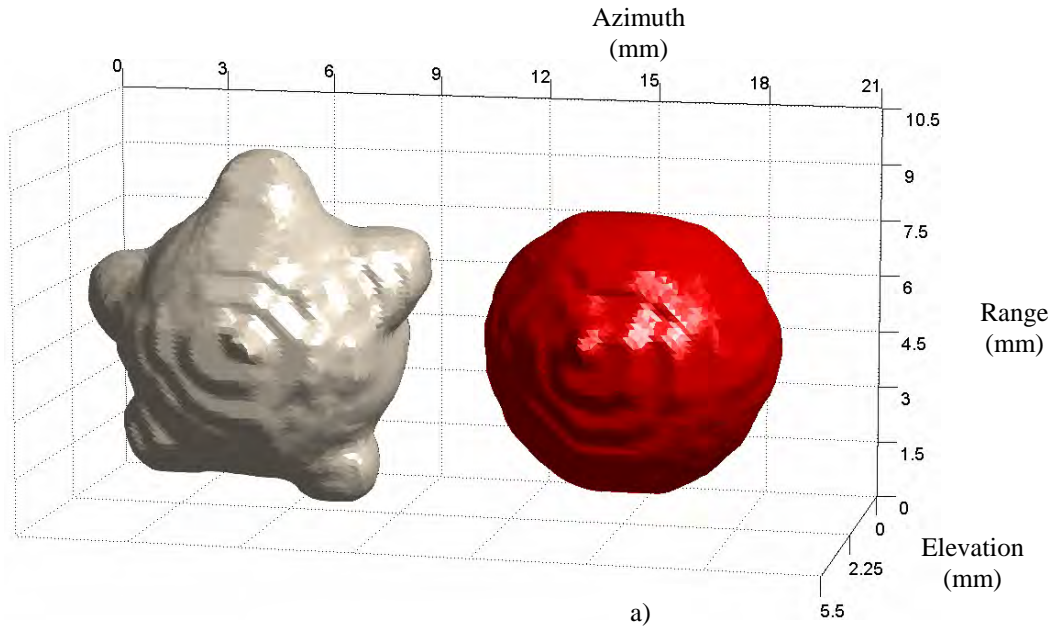
Figure 17: Lateral resolution simulation study: (a) 3D reconstruction from the reconstructed elastograms, (b) 3D reconstruction from numerical strain images derived from the FEA simulations.

2.   Elastographic phantom experiments for 3D rendering study

A. A purpose built prostate phantom

The acrylamide-based prostate phantom was fabricated using the protocol published by Negron et al. (2002). The prostate phantom consisted of three compartments - the prostate tissue with embedded inclusion, the anal passage, and the surrounding viscera. A schematic of the constructed phantom is illustrated in Figure 18, whereas Figure 19 illustrates a photographic view of the prostate phantom.
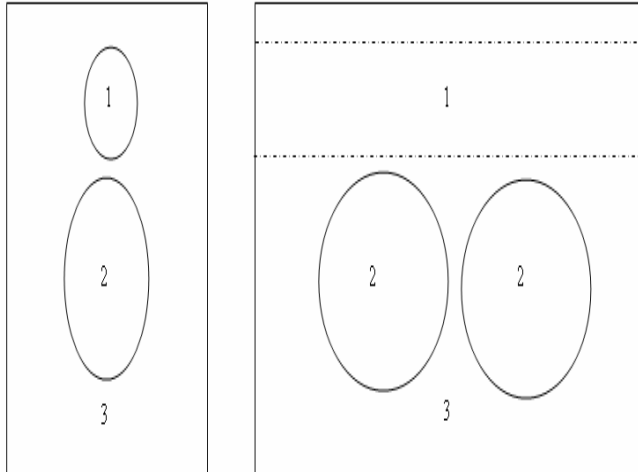
Figure 18: Schematic representation of the prostate phantom. 1: Anal passage, 2: Prostate tissue, 3:Viscera

Figure 19: Prostate phantom- a photographic view.

The prostate material and the surrounding gel (viscera) were composed of a 4% acrylamide solution, while inclusions in the prostates were composed of 8% acrylamide, which imparted different stiffness to the lesion and the surrounding prostate tissue. The Young's modulus for 4 % gel is approximately 4 KPa, whereas it is 16 KPa (Konofagou et al. 2003) in the 8% gel stiff inclusions. Thus, the modulus ratio for all embedded lesions was approximately four. Sephadex (GE-Amersham, Piscatway, NJ) was added to the prostates and inclusions to give speckle; a higher concentration of sephadex was added to the inclusions than the surrounding prostates, yielding a different speckle pattern. Two prostates of approximately 100 mL each were included in the phantom, one containing a spherical inclusions and the other containing an irregular inclusions. The smooth inclusion was approximately 8 mm in diameter whereas the irregular shaped inclusion had a mean diameter of 1 cm. To ensure uniform speckle-pattern in inclusions and prostate, the mixture of different component solutions was enclosed in a latex balloon and was rolled gently for a setting period (approximately 20 minutes following the mixing of components) until the solution had gelled. The rolling protocol mitigates against the settling of the embedded inclusion and may sometimes lead to a situation where two inclusions are placed apposing each other, hence two different prostates were constructed, each embedding one inclusion.

B. " I-Beam" transducer and elastographic phantom experiments

A Siemens Sequoia 512 scanner was used for image acquisition. The prostate phantom was scanned using an "I-Beam" type transducer - a modified linear transducer array consisting of a

central "imaging" array bordered by two perpendicular "tracking" arrays in a cylindrical housing, as illustrated in Figures 20 a-b. Using this configuration, the angular separation between two successive image slices could be tracked by measuring the azimuthal motion in the tracking arrays (Hossack et al. 2002, Garson et al. 2006). The arrays were operated at 12 MHz, using a -6 dB fractional bandwidth of approximately 40 %. A small tube for water delivery was attached to the transducer housing, and the assembly was surrounded with a water-tight latex transducer cover. When acquiring different image slices, the transducer had to be swept at an angle across the region of interest (ROI). This assembly was mounted so that during the angular rotation, translational motion was restricted, facilitating pure rotational motion of the transducer. The mounted transducer was inserted into the prostate phantom and used to perform a series of two-dimensional elastographic scans. At every angular position, the phantom was compressed by injecting water in the transducer sheath via the connected tube using a syringe pump while simultaneously collecting fifty I/Q data frames. For each lesion, gain, field of view, and focal depth were optimized for maximum visibility of that particular lesion. The data were processed offline as detailed in section 2 to generate elastographic image slices.
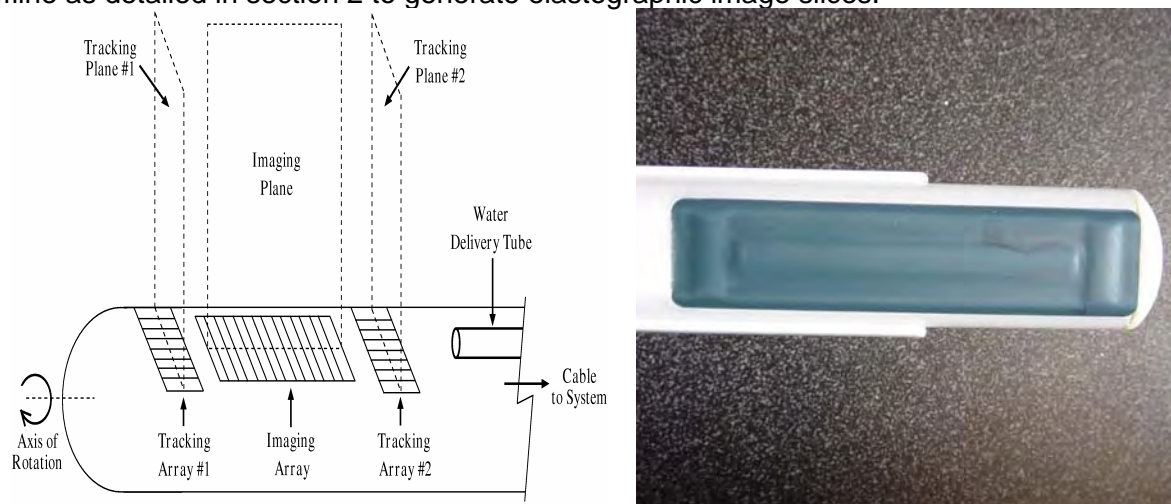

Figure 20: a) Configuration of the modified transducer comprising a central imaging array bordered by two perpendicular tracking arrays. During a scan, the transducer is rotated about its central axis, as indicated, b) A photographic view of prostate probe with tracking and imaging arrays.

C. Experimental results

Elastographic experiments were conducted as described in sub-section B. Both irregular shaped and smooth inclusions were imaged. Sixteen elastographic and sonographic image slices were acquired by sweeping the trans-rectal prostate transducer across the spatial extent of both inclusions. Figure 21 illustrates elastograms and corresponding sonograms for a few angular positions of the trans-rectal prostate transducer while sweeping across the irregular shaped inclusion. Figure 22 illustrates similar images for the smooth shaped inclusion. Figure 23 illustrates images of the smooth lesion reconstructed from sonograms and elastograms, respectively. The shape and the size of the smooth inclusion reconstructed from the sonograms and elastograms are approximately similar; the smooth inclusion reconstructed from elastograms tapers at the longitudinal edges, and is probably due to the low
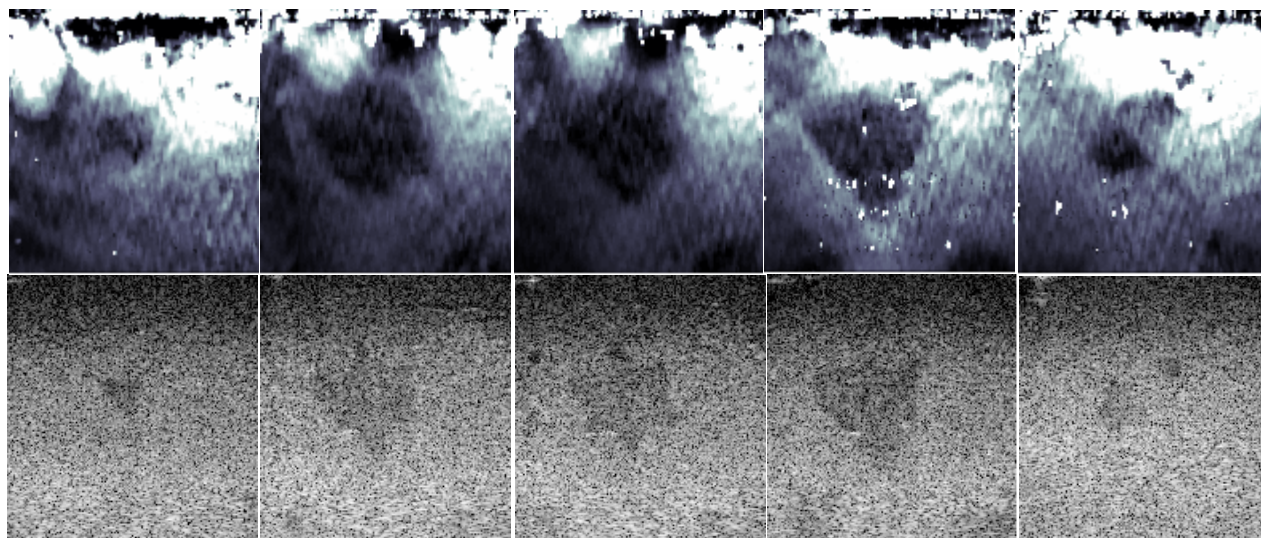
Figure 21: Few slices across the embedded inclusion mimicking a malignant lesion. Top row illustrates elastograms, bottom row illustrates sonograms. The field of view is 30 x 30 mm.
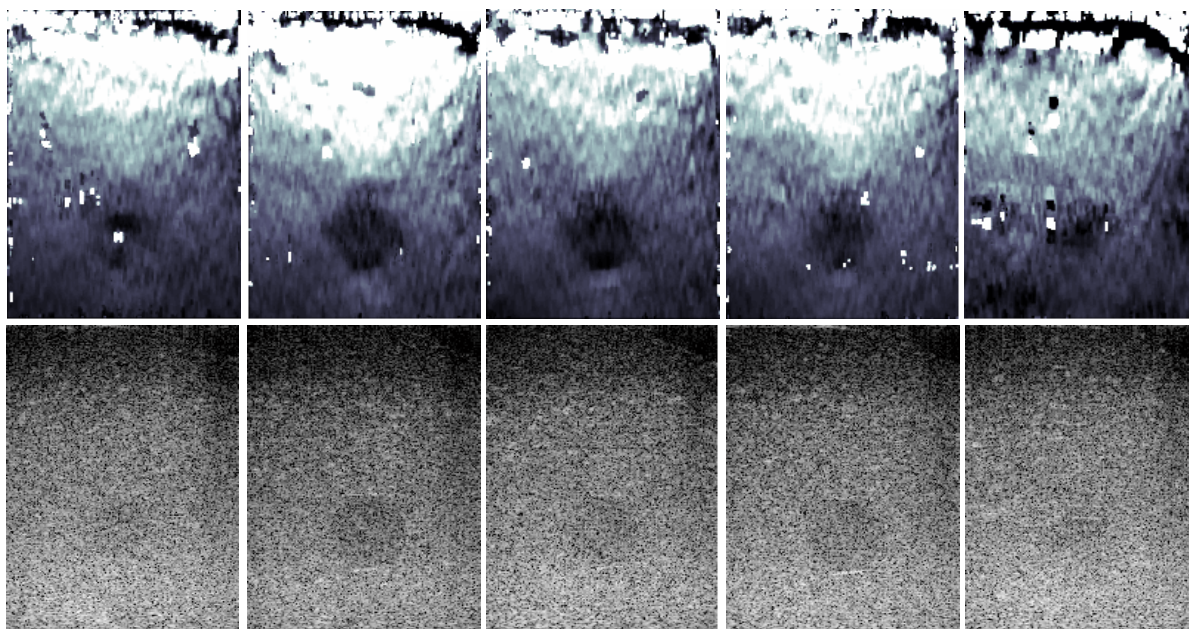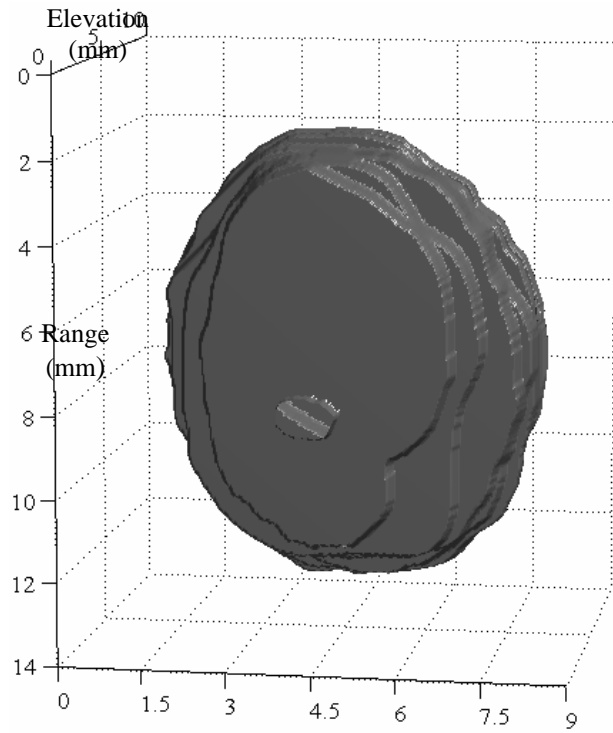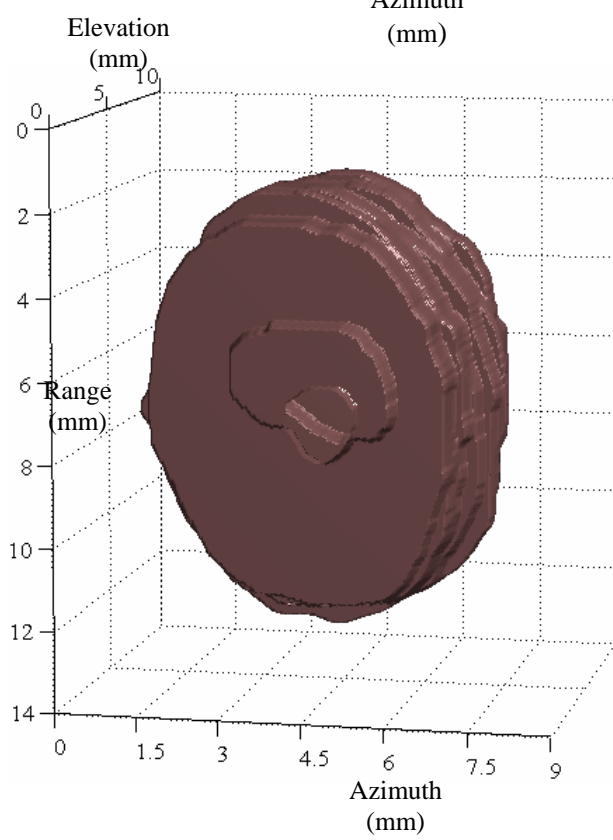

Figure 22: Few slices across the embedded inclusion mimicking a benign lesion. Top row illustrates sonograms, bottom row illustrates elastograms. The field of view is 40 x 30 mm.

Figure 23: a) Smooth inclusion mimicking a benign lesion reconstructed from elastograms. b) Smooth inclusion reconstructed from sonograms.

pass filtering or smoothing effect of the processing windows used for generating elastograms (Srinivasan et al 2002a,). Figure 24 illustrates the irregular shaped lesion reconstructed from the elastograms and sonograms, respectively. The shape of the irregular shaped inclusion, when reconstructed from the elastograms, has blunt edges and appears larger in size than that reconstructed from the sonogram or B-mode image. Similar results have been reported by Garra et al. (1997) where the authors demonstrate the same by comparing the sonographic and elastographic images for an irregular shaped malignant cancer in in-vivo human scans. Thus, we contend that the 3D size and the shape of the reconstructed lesion (inclusion) have the potential to assist in discriminating benign cancers from malignant cancers.
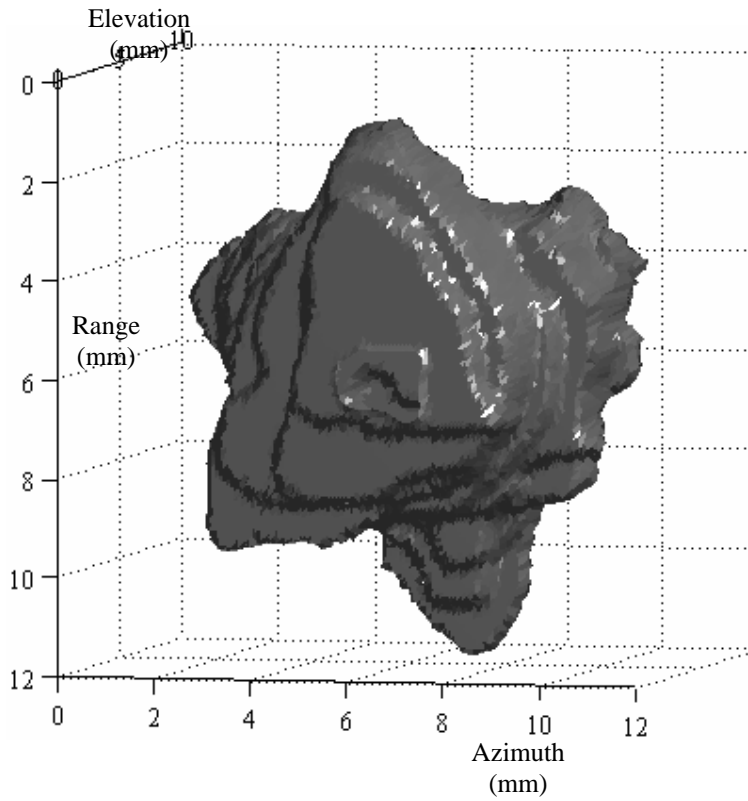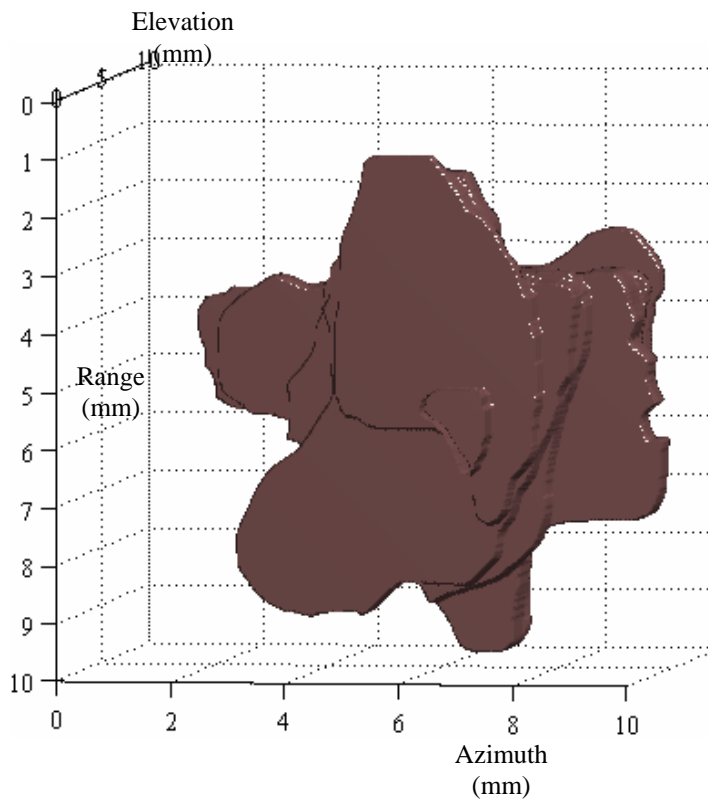
Figure 24: a) Irregular shaped inclusion mimicking a malignant lesion reconstructed from elastograms. b) Irregular shaped lesion inclusion reconstructed from sonograms.

Discussion

In elastography, image quality is contingent upon accurate estimation of internal tissue displacements. Signal companding is a simple, yet elegant, approach of improving elastographic image quality. In the second section of this article, we proposed an adaptive stretching based tracking algorithm. The algorithm takes into account the local variations in tissue elasticity and performs iterative local stretching, which provides a superior CNR_e to previously proposed adaptive tracking algorithms (Srinivasan et al. 2002b). When encountering non-uniform boundary conditions, as in prostate elastography, the proposed algorithm is expected to perform better than conventional stretching based algorithms as they require an *a priori* estimate of the applied strain. When using an ultrasound scanner operating at higher frame rates with a high bandwidth transducer and performing handheld or trans-rectal prostate elastography, the net motion between the consecutive image frames may be small. Thus, the correlation-based tracking in the first two stages of this algorithm may be replaced by a sum-of-absolute-difference approach (Chaturvedi and Insana 1999), whereas the third stage may be replaced by temporal tracking of zero crossings (Srinivasan et al.2002b) of the pre- and post-compression echo RF signals. Thus, a reduction in computation time may be achieved by an order of magnitude without any substantial degradation in image quality. Such a modified algorithm, when implemented on FPGA's, can be easily incorporated into programmable scanners such as the ULTRASONIX RP (Richmond, BC) and may help in real time tissue elasticity imaging. In a PC based environment, real-time image registration and rendering algorithms (Tay et al. 2006) may be used to render multiple image slices to accurately reconstruct a 3D volumetric elastogram. For this work, the elevational resolution is expected to be a function of the greater of the two properties of the data set, the elevational beam width and the angular separation between two consecutive slices and intuitively may be assumed to be a linear function of depth as the separation between two consecutive slices increases linearly as a function of depth. Thus, for detecting and rendering smaller lesions deep in tissue, it may be essential to have sufficiently high angular sampling in addition to having a higher image frame rate. Nevertheless, such 3D elastography imaging systems may be used for a variety of applications such as real-time volumetric monitoring of HIFU lesions (Souchon et al. 2005), real-time volumetric estimation of viscous properties of tissue using non-linear or sinusoidal compression techniques between consecutive image frames thereby imaging the temporal behavior of the tissue strain (Erpelding et al. 2005), and temporal monitoring of the growth of cancers.

Aim 3. Apply image processing algorithms to acquired B-Mode and elasticity images to improve the quantification of detected elastic inhomogeneities

Image Processing and Quantification

We have progressed to a accurate 3D surface rendering from 2D slices by implementing a 3D gradient vector flow (GVF) snake algorithm (Xu and Prince 1998). The 2D and 3D GVF snake algorithm relies on the edges to be well delineated and contrast between the various regions to be well defined in each 2D ultrasound slice to produce a surface that resembles the actual scanned object. In ultrasound, images are affected by a granular interference pattern known as "speckle". Before an accurate 3D surface rendering can be attained,a preprocessing despeckling step is needed to reduce the variances in pixel values within homogeneous regions while contrast between distinct regions are concurrently enhanced. We have evaluated a wide variety of well known methods such as the Nagao and Matsuyama filter (Nagao and Matsuyama 1979), the Lee filter(Lee 1980), the Frost *et al.* filter (Frost, Stiles et al. 1982), the Kuan *et al.* filter (Kuan, Sawchuk et al. 1985), the adaptive weighted median filter proposed by Loupas *et al.*(Loupas, McDicken et al. 1989), the Wiener filter (Kailath 1976) SRAD proposed by Yu and Acton (Yu and Acton 2002), and a novel stochastically driven method design specifically for 3D surface rendering from 2D slices of the prostate and other organs. The method we develop specifically for the task of this grant is a stochastically driven compression filter called the "squeeze box filter" (SBF). Our quantitative evaluation using a Field II (Jensen and Svendsen 1992) simulated B mode ultrasound image with contrast enhancement performance determined by a modified Fisher discriminant has determined that the newly developed SBF method outperformed the other methods and is exceptional in providing the needed intra-region reduction in variance and inter-region contrast enhancement with computational efficiency. In Figs. 25, 26, and 27, we show the 3D surface, the side view, and the bottom view, respectively, of the rendering we attained from a sequence of scans we acquired of an egg phantom. The sequence consists of acquiring a 2D slice every millimeter along the long axis of an egg phantom. We processed each slice with the SBF despeckling method. The 3D rendering was attain by SBF processing each slice then applying a 3D GVF snake to attain the final results shown in Fig. 13, 14, and 15. It is very evident that our method captured the essential size and shape of the egg phantom.
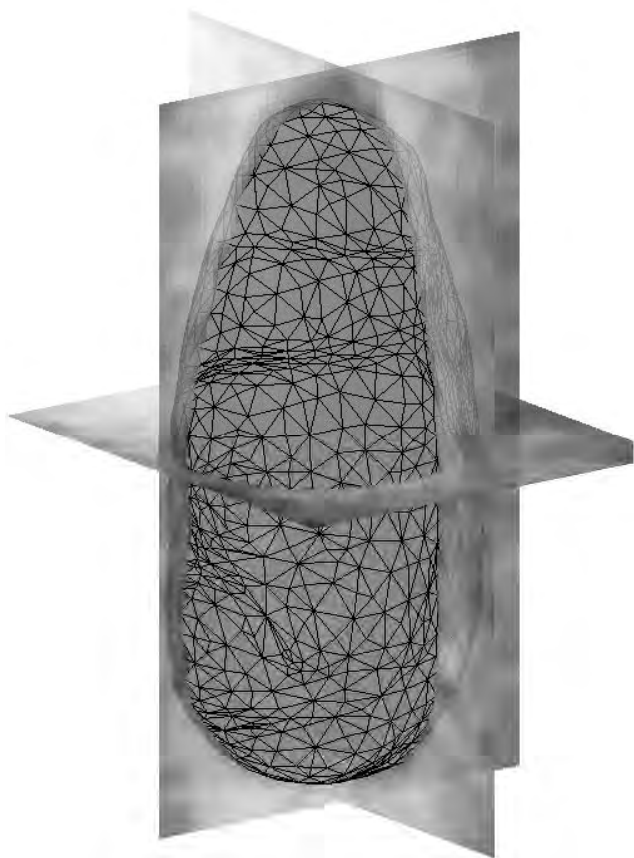
Figure 25. 3D surface found by the 3D GVF with slices preprocessed by SBF.
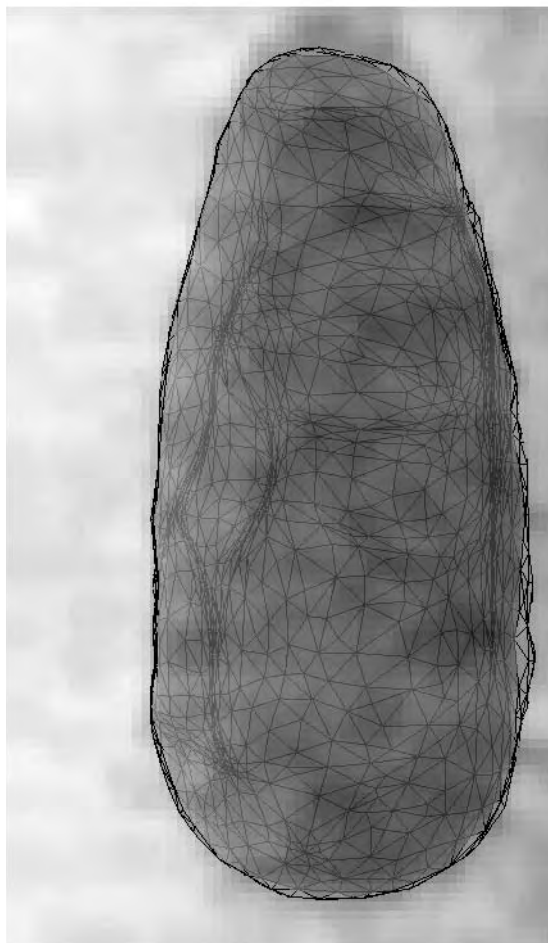
Figure 26. Side view of the surface rendered by the 3D GVF snake
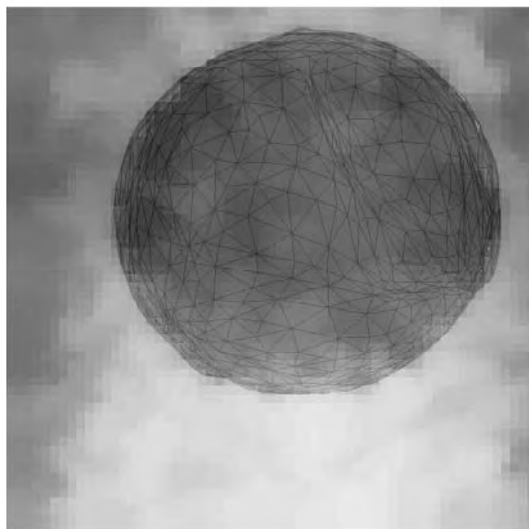with slices preprocessed by SBF.

Figure 27. Bottom view of the surface of the egg phantom
rendered by the 3D GVF snake with slices preprocessed by SBF.

After the 3-D surface of the prostate is segmented, the volume is determined by applying a novel blobbing technique, called the multi-directional connected component analysis (MDCCA). The MDCCA requires that the surface, which is represented by a set of 3-D vertices and faces, to be densely meshed so that each vertex is no more than one voxel from its neighboring vertices. A 2-D binary image of the contour is defined by the intersection of a plane through the densely mesh surface. This binary image is zero except when the pixel lies on the contour, in which case the pixel is set at one. The interior enclosed by the 2-D close contour is determined by extracting the connected component in several directions and applying a logical "and" operator to the resulting binary images. A connected component binary image in some fixed direction is the result of approaching the 2-D closed contour in some fixed direction, say left to right in each row or top to bottom in each column for examples, and setting the pixel values to zero until a contour pixel is reached, in which case the remaining pixels in the fixed direction are set to one. Fig. 28 shows the connected component binary images in eight directions. Fig. 29 shows the result of applying a logical "and" operator to the eight binary images in Fig. 28. The MDCCA of non-intersecting slices through the 3-D densely meshed surface yields a binary 3-D data where the voxels are one when the voxel lies within the interior of the 3-D surface and zero otherwise. An example of a binary 3-D data produced by applying the MDCCA to non-intersecting slices is shown in Fig. 30. The volume in units of voxels of the object enclosed by the 3-D surface is attained by summing the binary 3-D data of MDCCA of non-intersecting slices. The volume is converted to units of cubic centimeter (or millimeter or other units) by multiplying with the voxel resolution.
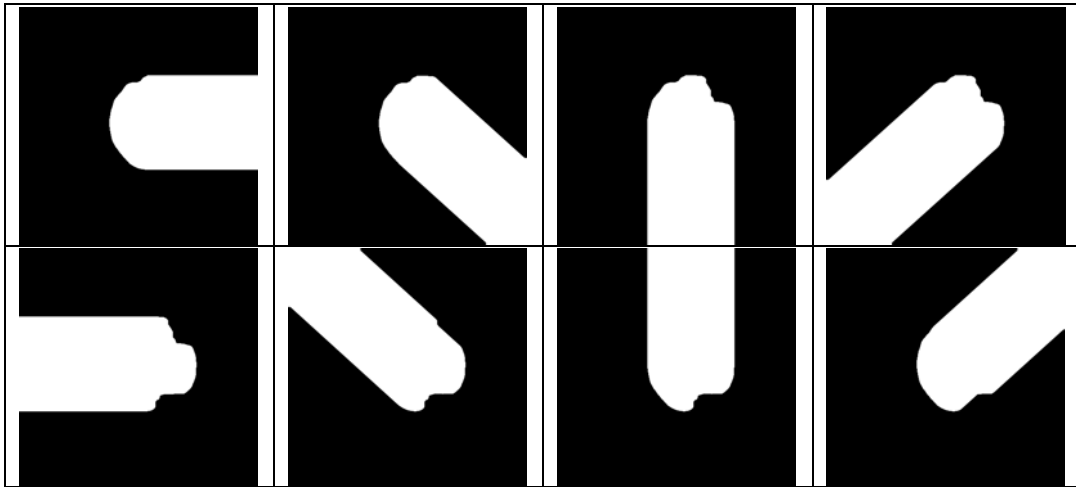

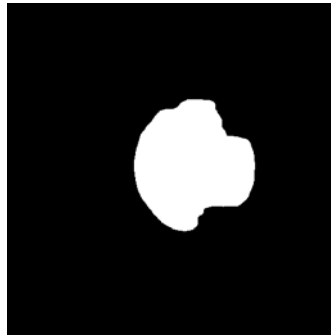Figure 28. Connected components in eight directions.

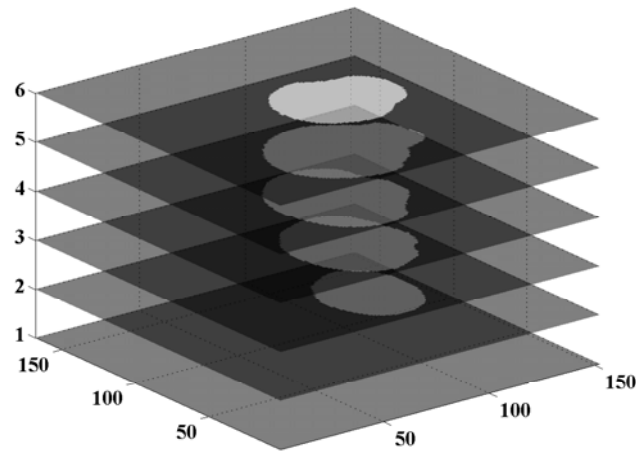Figure 29. Connected components in eight directions.

Figure 30. MDCCA of non-intersecting slices.

Papers of our novel methods have been published in the Proceedings of the **2006 IEEE International Symposium for Biomedical Imaging: From Nana to Macro** and the Proceedings of the **IEEE International Conference on Image Processing 2006**. A journal papers of our despeckling, surface segmentation, and volume calculation (MDCCA) methods have been submitted to Elsevier DSP, Elsevier Computerized Medical Imaging and Graphics, and IEEE Transactions in Medical Imaging

Excellent progress with respect to Aim 3 has been made in the third year of the grant.

The fourth Aim from the Statement of Work relates to a small scale clinical validation in collaboration with partially funded University of Virginia collaborator – Dr. Dan Theodorescu. In the third year of the grant we worked to resolve issues with obtaining a joint US DoD and UVA IRB approval. We believe that the protocol and patient consent forms are in order and are pending acceptance. We filed for a no cost extension to allow for completion of the proposed research – i.e. the small scale clinical validation. The small scale clinical validation and any subsequent report/ paper will probably mark the conclusion of the funded and reportable work in this grant.

KEY RESEARCH ACCOMPLISHMENTS

- We have largely completed Aims 1, 2 and 3. Specifically, we have designed and had fabricated a very high resolution transrectal ultrasound transducer array for high resolution prostate imaging.
- We have integrated the new transducer with an ultrasound scanner and an automated injection stage to realize an accurate elastographic imaging device.
- We have tested the 3D and elastographic imaging capability of the transducer / scanner.
- We have developed new ultrasound speckle reduction techniques suitable for prostate ultrasound
- We have developed new ultrasound signal tracking techniques that improve the quality of ultrasound derived 3D measures of elastic anomaly as might be very useful in the more sensitive and more specific detection of prostate cancer.

REPORTABLE OUTCOMES

Y. Li, A. Patil and J. A. Hossack, "**High resolution three-dimensional prostate ultrasound imaging**". Proc. SPIE Medical Imaging, San Diego, CA, 2006

A. Patil, C. D. Garson, M. A. Oberhardt, P. C. Tay, and J. A. Hossack "**3D Prostate Elastography: Simulations and Experiments"** Proc. of the 2006 IEEE International Ultrasonics Symposium, 2006, P1230-1233

A. Patil, C. D. Garson, M. A. Oberhardt, P. C. Tay, and J. A. Hossack "**Multi-Resolution Hybrid Strain Estimator for Elastography**" Proc. of the 2006 IEEE International Ultrasonics Symposium, 2006, P1258-1261

P. C. Tay, S. T. Acton and J. A. Hossack, "**A stochastic approach to ultrasound despeckling**", Proc. of the 2006 IEEE International Symposium for Biomedical Imaging: From Nana to Macro Arlington, VA, 2006, pp. 221-224

P. C. Tay, S. T. Acton and J. A. Hossack, "**Ultrasound Despeckling Using An Adaptive Window Stochastic Approach",** Proc. of the IEEE International Conference on Image Processing 2006, pp. 2549-2552

P. C. Tay, S. T. Acton and J. A. Hossack, "**An outlier removing signal reconstruction method"**, under review at Elsevier DSP

P. C. Tay, B. Li, C. D. Garson, S. T. Acton and J. A. Hossack, "**Ultrasound despeckling for 3-D segmentation",** under review at IEEE Transaction on Medical Imaging

P. C. Tay, S. T. Acton and J. A. Hossack, "**An outlier removing signal reconstruction method"**, under review at Elsevier DSP

P. C. Tay, B. Li, C. D. Garson, S. T. Acton and J. A. Hossack, "**Ultrasound despeckling for 3-D segmentation",** under review at IEEE Transaction on Medical Imaging

CONCLUSIONS

Our prostate imaging approach combines using an I-Beam transducer with 3D capability, elasticity imaging and test on a prototype using a prostate tissue-mimicking phantom. The prostate strain imaging performed here using a slightly inflated sheath over the transrectal transducer significantly enhanced tumor visibility (a hard inclusion in the phantom). (The lesion was nearly invisible in the regular B-mode image.) The I-Beam transducer enabled reconstruction of discrete 2D image acquisitions into regular 3D grid space, and thus the tumor was rendered in 3D. The volume calculated for this tumor had an error of approximately 11% compared to the actual (independently determined) volume. Additionally, we have made significant progress in the area of image pre-processing (i.e. speckle reduction) and in image quantification (i.e. feature segmentation). These image processing contributions significantly enhance the practical utility of our technique since they hold the promise of accelerating the

prostate cancer diagnostic task and reducing intra and inter operator variability. Reducing variability has significance since serial analysis of cancer growth or remission is dependent on accurate and repeatable measures of prostate volume. Since we are able to measure volumes directly, rather than extrapolating volume from a length dimension or cross-sectional area, our image contributions are well-matched and complement our contributions in 3D and elastographic imaging.

"So what? Section"

Our improved prostate ultrasound imaging techniques have the potential to detect prostate cancer earlier and with more reliability (i.e. improved sensitivity and specificity). In this way, we believe that our research has a useful public health contribution.

REFERENCES:

American Cancer Society, Statistics from www.cancer.org, 2006.

Bilgen, M., and Insana, M.F., "Predicting target detectability in acoustic Elastography", Proceedings of IEEE Ultrasonic Symposium, 2: 4217-1430, 1997.

Bilgen, M., "Wavelet transform based strain estimator for Elastography", IEEE Trans. on UFFC, 46(6): 1407-1415, 1999.

Céspedes, I. and Ophir, J., "Reduction of image noise in elastography", Ultrasonic Imaging, 15 (2): 89-102, 1993.

Chaturvedi, P., Insana, M.F., and Hall, T.J., "2-D companding for noise reduction in strain imaging", IEEE Trans. on UFFC, 45(1): 179-191, 1999.

Chen, E.J., Jenkins, W.K., and O'Brien, W.D., Jr., "The accuracy and precision of estimating tissue displacements from ultrasonic images", Proceedings of IEEE Ultrasonic Symposium, 2: 1069-1072, 1992.

Cochlin, D. L., Ganatra R. H., and Griffiths, D. F. R., "Elastography in detection of prostatic cancer", Clinical Radiology, 57: 1014-1020, 2002.

Elkis, M. J., and Brawer, M. K., "The significance of iso-echoic prostate carcinomas", Urology, 152: 2304-2307, 1994.

Elman, H. C., "Preconditioned Conjugate-Gradient Methods for Nonsymmetric Systems of Linear Equations", Advances In Computer Methods for Partial Differential Equations IV, Vichnevetsky, R., Stepleman, ed., IMACS, 409-413, 1981.

Erpelding T. N., Hollman K. W., and O'Donnell M., "Bubble-based acoustic radiation force elasticity imaging", IEEE Trans. on UFFC, 52(6): 971-979, 2005.

Fellepa, E. J., Ennis, R. D., Schiff, P. B., Wuu, C. S., Kalisz, A., Ketterling, J., Urban, S., Liu, T., Fair, W. R., Porter, C. R., and Gillespie, J. W., " Spectrum-analysis and neural networks for imaging to detect and treat prostate cancer", Ultrasonic Imaging, 23: 135-3146, 2001.

Frauscher, F., Klauser, A., Halpern, E. J., Wolfgang, H., Bartsch, G., "Detection of prostate cancer with a microbubble ultrasound contrast agent" , The Lancet, 35:1849-1850, 2001.

Fung, Y., C., "Biomechanical properties of Living Tissue", Chapter 7, Springer Publications, NewYork, 1984.

Garra, B.S., Céspedes, I., Ophir, J., Spratt, S., Zuurbier, R. A., Magnant, C. M., and Pennanen, M. F., "Elastography of Breast lesions: initial clinical results", Radiology, 202: 79-86, 1997.

Garson, C. D., Li Y., and Hossack, J. A., " Free hand scanning approaches for volume quantification of the mouse heart left ventricle", submitted to IEEE Trans. on UFFC, 2006.

Halpern, E. J., MCcue, P. A., Aksnes, A., K., Hagen. E. K., Frauscher, F., and Gomella, L. G., "Contrast-enhanced US of prostate with Sonazoid: Comparision with Whole-Mount prostatectomy specimens in 12 patients", Radiology, 222(2): 362-366, 2002.

Hossack, J.A., Sumanaweera, T.S., Napel, S., and Ha, J.S, "Quantitative 3D Diagnostic Ultrasound Imaging Using a Modified Transducer Array and an Automated Image Tracking Technique", IEEE Trans. on UFFC, 49(8): 1029-1038, 2002.

Jensen J. A., and Nikolov, I., "Fast simulations of Ultrasound images", Proceedings of IEEE Ultrasonic Symposium, 2: 1721-1724, 2000.

Kallel, F., and Ophir, J., "A least squares estimator for elastography" Ultrasonic Imaging, 19(3): 195-208, 1997.

Kasai, C., Namekawa, K., Koyano, A., and Omoto, R., "Real-time two dimensional blood flow imaging using an autocorrelation technique", IEEE Trans. on UFFC, 32(3): 458-464, 1985.

Konofagou, E. E., Varghese, T., and Ophir, J., "Spectral Estimators in Elastography", Ultrasonics, 38(1): 412-416, 2000a.

Konofagou, E. E., Varghese, T., and Ophir, J., "Theoretical Bounds on the Estimation of Transverse Displacement, Transverse Strain and Poisson's Ratio in Elastography", Ultrasonic Imaging, 22(3): 153-177, 2000b.

Konofagou, E. E., Ottensmeyer M., Dawson S. L., and Hynynen K., " Harmonic motion imaging- Applications in detection of stiffer masses." , Proceedings of IEEE Ultrasonic Symposium, 558-561, 2003

Krouskop, T. A., Wheeler, T. M., Kallel, F., Garra, B. S., and Hall, T., "Elastic Moduli of Breast and Prostate Tissues under Compression", Ultrasonics Imaging, 20: 260-274, 1998.

Lee, F., Littrup, P. J., Torp-Pederson, S. T., Mettlin, C., McHugh, T. A., Gray, J. M., Kumasaka, G. H., and Mcleary, R. D., " Prostate cancer: Comparison of trans-rectal Ultrasound and digital rectal exam for screening", Radiology, 168(2): 389-394, 1988.

Li, Y., Patil, A. V., and Hossack, J.A., "Combined elasticity and 3D imaging of the prostate", Proceedings of IEEE Ultrasonic Symposium, 3: 1435-1438, 2005.

Liu, J., Abbey, C. K., and Insana, M. F., "Linear approach to resolution in elasticity imagining", IEEE Trans. on UFFC, 51(6): 716-725, 2004.

Negron, L.A., Viola, F., Black, E.P., Toth, C.A., and Walker, W.F, "Development and characterization of a vitreous mimicking material for radiation force imaging", IEEE Trans. on UFFC, 49(11): 1543-1551, 2002.

Nightingale, K. R, Nightingale R. W., Palmeri, M. L., and Trahey, G. E., "A Finite Element Model of Remote Palpation of Breast Lesions Using Ultrasonic Radiation Force: Factors Affecting Tissue Displacement" , Ultrasonic Imaging, 22(1): 35-54, 2000.

O'Donnell, M., Skovoroda, A. R., Shapo, B. M., and Emelianov, S.Y., "Internal displacement and strain imaging using ultrasonic speckle tracking", IEEE Trans. on UFFC, 41 (3): 314-325, 1994.

Ophir, J., Céspedes, I., Ponnekanti, H., Yazdi, Y., and Li., X., "Elastography: A method for imaging the elasticity of biological tissue", Ultrasonic Imaging, 13(2): 111-134, 1991.

Patil, A., V., "Quantitative comparison of 2D and 3D elastograms: A simulation study", Masters' Thesis, University of Houston, 2005.

Patil A.V., Krouskop, T. A., Ophir, J., and Srinivasan, S., "On the effect of 3D tissue motion on Ultrasound Elastography: A simulation study", submitted to Physics in Medicine and Biology, 2006.

Pesavento, A., and Lorenz, A., "Real time strain imaging and in-vivo application in prostate cancer", Proceedings of IEEE Ultrasonic Symposium, 1647-1652, 2001.

Potdevin, T., Moskalik, A., Rubin, M., Bree, R., and Carson, P., "Zonal Analysis of 3D Ultrasound Doppler Quantitative Measure for the Discrimination of Prostate Cancer", Proceedings of IEEE Ultrasonic Symposium, 1321-1324, 2000.

Shapo, B.M., Crowe, J.R, Skovoroda, A.R., Eberle, M.J., Cohn N.A., and O'Donnell, M. ," Displacement and Strain Imaging of Coronary Arteries with Intraluminal Ultrasound", IEEE Trans. on UFFC, 43: 234-240, 1996.

Sheppard, M. A., and Shih, L., "Efficient Image texture analysis and classification for prostate cancer diagnosis", Proceedings of IEEE computational systems workshop, 2005.

Souchon, R., Bouchoux, G., Maciejko, E., Lafon, C., Bertrand, M., and Chapelon, J. Y., "Monitoring the formation of thermal lesions with heat-induced echo-strain imaging: A feasibility study", Ultrasound in Medicine and Biology, 31(2): 251-259, 2005.

Srinivasan, S., Ophir, J., and Alam, S.K., "Elastographic Imaging Using Staggered Strain Estimates", Ultrasonic Imaging, 25: 229-245, 2002a

Srinivasan, S., Kallel, F., Souchon, R., and Ophir, J., "Analysis of an Adaptive Strain Estimation Technique in Elastography", Ultrasonic Imaging, 24(2): 109-118, 2002b.

Tay, P. C., Li, B., Garson, C. D., Acton, S. T., and Hossack, J., A., "Left ventricle reconstruction and volume estimations using model fitting and active surface", submitted to IEEE Trans. on image processing, 2006.

Techavipoo, U., Chen, Q., Varghese, T., and Zagzebski, J.A., "Estimation of displacement vectors and strain tensors in elastography using angular insonifications", IEEE Trans. on Medical Imaging, 23(12): 1479-1484, 2004.

ThitaiKumar, A., Ophir, J., and Krouskop, T. A., "Noise performance and signal-to-noise ratio of shear strain elastograms", Ultrasonic Imaging, 27: 145-165, 2005.

Ueno E., "Classification and Diagnostic criteria in breast echography", Japanese Journal on Medical Ultrasonic, 13: 19-31, 1986

Varghese, T., and Ophir, J., "A theoretical framework for performance characterization of elastography: The Strain Filter", IEEE Trans. on UFFC, 44: 164-172, 1997.

Viola, F., and Walker, W.F., "Shear strain Elastography", Proceedings of IEEE Ultrasonic Symposium, 1907-11, 2002.

Walker, F., W., Trahey, G., E., " A fundamental limit on delay estimation using partially correlated speckle signals", IEEE Trans. on UFFC, 42: 301-308, 1995.

Walker, W. F., "A spline based approach for computing spatial impulse responses", submitted to IEEE Trans. on UFFC, 2006.

Waterhouse, R. L., and Resnick, M. I., "The use of trans-rectal prostatic ultrasonography in the evaluation of patients with prostatic carcinoma", Urology, 141 (2): 233-239, 1989.

Clements, R. (2002). "The Role of Transrectal Ultrasound in Diagnosing Prostate Cancer." Current Urology Reports 3: 194-200.

Crawford, E., S. Leewansangtong, et al. (1999). "Efficiency of Prostate-Specific Antigen and Digital Rectal Examination in Screening, Using 4.0 ng/mL and Age Specific Reference Range as a Cutoff for Abnormal Values." The Prostate 38: 296-302.

Frauscher, F., A. Klauser, et al. (2001). "Detection of Prostate Cancer with a Microbubble Ultrasound Contrast Agent." The Lancet 357: 1849-1850.

Frost, V., J. Stiles, et al. (1982). "A model for radar images and its applicationto adaptive digital filtering of multiplicative noise,." IEEE Trans. Pattern Anal. Machine Intell 4(2): 157-166.

Halpern, E., P. McCue, et al. (2002). "Contrast-enhanced US of the Prostate with Sonozoid: Comparison with Whole-Mount Prosatectomy Specimens in 12 Patients." Radiology 222: 361-366.

Jensen, J. and N. Svendsen (1992). "Calculation of Pressure Fields from Arbitrarily Shaped, Apodized and Excited Ultrasound Transducers." IEEE Transactions on Ultrasonics Ferroelectrics & Frequency Control 39: 262-267.

Kailath, T. (1976). "Equations of Wiener-Hopf type in filtering theory and related applications." Norbert Wiener: Collected Works vol. III, P. Masani, Ed., Cambridge, MA: MIT Press: 63-94.

Kuan, D., A. Sawchuk, et al. (1985). "Adaptive noise smoothing filter for images with signal-dependent noise." IEEE Trans. Pattern Anal. Machine Intell 7(2): 165-177.

Lee, J. (1980). "Digital image enhancement and noise filtering by use of local statistics." IEEE Trans. Pattern Anal. Machine Intell 2(2): 165-168.

Loupas, T., W. McDicken, et al. (1989). "An adaptive weighted median filter for speckle suppression in medical ultrasonic images." IEEE Trans. Circuits Syst. 36(1): 129-135.

Nagao, M. and T. Matsuyama (1979). "Edge preserving smoothing." Computer Graphics and Image Processing 9(4): 394-407.

Negron, L., F. Viola, et al. (2002). "Development and characterization of a vitreous mimicking material for radiation force imaging." IEEE Transactions Ultrasonics, Ferroelectrics and Frequency Control 49(11): 1543-1551.

Sarvazyan, A. (1998). "Mechanical imaging: a new technology for medical diagnostics." Journal of Medical Informatics 49(2): 195-216.

Society, A. C. (2004). "American Cancer Society Prostate Cancer Statistics from www.cancer.org."

Taylor, J., K. Gancarczyk, et al. (2002). "Increasing the number of core samples taken at prostate needle biopsy enhances the detection of clinically significant prostate cancer." Urology 60(5): 841-845.

Toubert, M., M. Schlageter, et al. (1990). "Screening for cancer of the prostate using prostate-specific antigen." Presse Medicale 19(24): 1139-1142.

Weiss, R., V. Hartanto, et al. (2001). "In vitro trial of the pilot prototype of the prostate mechanical imaging system." Urology 58(6): 1059-1063.

Xu, C. and J. Prince (1998). "Snakes, Shapes and Gradient Vector Flow." IEEE Trans. Image Processing 7(3): 359-369.

Yu, Y. and S. Acton (2002). "Speckle reducing anisotropic diffusion." IEEE Transactions on Image Processing 11: 1260-1270.